Title
Continuum approach for modeling and simulation of fluid diffusion through a porous finite elastic solid

Permalink
https://escholarship.org/uc/item/1cp328r3

Author
Zhao, Qiangsheng

Publication Date
2013

Peer reviewed|Thesis/dissertation

Continuum approach for modeling and simulation of fluid diffusion through a porous finite elastic solid

by

Qiangsheng Zhao

A dissertation submitted in partial satisfaction of the requirements for the degree of

Doctor of Philosophy

in

Engineering - Mechanical Engineering

in the

Graduate Division

of the

University of California, Berkeley

Committee in charge:

Professor Panayiotis Papadopoulos, Chair
Professor Tarek Zohdi
Professor James Sethian

Fall 2013

Continuum approach for modeling and simulation of fluid diffusion through a porous finite elastic solid

Copyright © 2013

by

Qiangsheng Zhao

Abstract

Continuum approach for modeling and simulation of fluid
diffusion through a porous finite elastic solid

by

Qiangsheng Zhao

Doctor of Philosophy in Mechanical Engineering

University of California, Berkeley

Professor Panayiotis Papadopoulos, Chair

The diffusion of liquid and gas through porous solids is of considerable technological interest and has been investigated for decades in a wide spectrum of disciplines encompassing chemical, civil, mechanical, and petroleum engineering. Porous solids of interest are made of either natural materials (e.g., soil, sand) or man-made materials (e.g., industrial filters, membranes). In both cases, liquids (e.g., water, crude oil) and gases (e.g., air, oxygen, natural gas) are driven through the voids in the porous solid by naturally or artificially induced pressure. Nafion$^{®}$ is an important example of a well-characterized man-made porous medium due to its extensive use in proton-exchange membrane fuel cells. Here, while the fuel cell is in operation, a mixture of air and water diffuses through the pores of a Nafion$^{®}$ membrane. The efficiency of the fuel cell is affected by the variation in water concentration. In addition, high water concentration has been experimentally shown to cause substantial volumetric deformation (swelling) of the membrane, which may compromise the integrity of the device.

In this dissertation, a continuum approach for modeling diffusion of fluid through a porous elastic solid is proposed. All balance laws are formulated relative to the frame of a macroscopic solid resulting from the homogenization of the dry solid and the voids. When modeling only liquid diffusion through the macroscopic solid, the displacement of the macroscopic solid and the liquid volume fraction are chosen to characterize the state of the porous medium, and Fick's law is used as the governing equation for liquid flow. When modeling multiphase diffusion through the macroscopic solid, the displacement of the solid, the gas pressure and the liquid saturation are chosen as state variables, and both fluid diffusions are assumed to follow Darcy's law. Both single phase and multiphase diffusion models are implemented in the finite element method, and tested with various loading conditions on different types of materials. Numerical simulation results are presented to show the predictive capability of the two models.

Acknowledgements

Contents

List of Figures

iv

Chapter 1

Introduction

The diffusion of liquid and gas through porous solids is of considerable technological interest and has been investigated for decades in a wide spectrum of disciplines encompassing chemical, civil, mechanical, and petroleum engineering. Porous solids of interest are made of either natural materials (e.g., soil, sand) or man-made materials (e.g., industrial filters, membranes). In both cases, liquids (e.g., water, crude oil) and gases (e.g., air, oxygen, natural gas) are driven through the voids in the porous solid by naturally or artificially induced pressure. Nafion$^{\circledR}$ is an important example of a man-made porous medium due to its extensive use in proton-exchange membrane fuel cells. Here, while the fuel cell is in operation, a mixture of air and water diffuses through the pores of a Nafion$^{\circledR}$ membrane. The efficiency of the fuel cell is affected by the variation in water concentration [38, 37]. When the water concentration is too high, the two electrodes are flooded and catalysts are incapacitated, hence retarding (or even completely arresting) the chemical reactions. On the other hand, when the water concentration is too low, the membrane dries up and this limits the conductivity of protons.

The transport of the liquid phase and its interaction with the solid phase have been studied by different mechanical theories. Among them, mixture theory was one of the earliest to be investigated. This theory was originally proposed by Fick [21] in his work on diffusion. Truesdell [50] proposed the earliest phenomenological continuum theory of mixture. The theory was further refined in a series of subsequent contributions, see, e.g., [4, 5, 6, 40]. In particular, Adkins [1, 2, 3] and Bowen [10, 11] studied flow through porous media using mixture theory. In mixture theories, it is assumed that different constituents coexist in an infinitesimal volume at any point and at any time in the body. Each constituent has its own motion, and time derivatives of its physical properties are calculated according to this motion. Mass balance laws are formulated for each constituent in a classical fashion, although balance of linear momentum includes interaction forces due to the other constituents. The field equations are derived through averaging procedures for each constituent. Mixture theory provides a framework for formulating balance laws of multiphase system, but in order to close the system of equations, additional constitutive assumptions are required. Mixture theory suffers from the major drawback of requiring separate boundary conditions for each con-
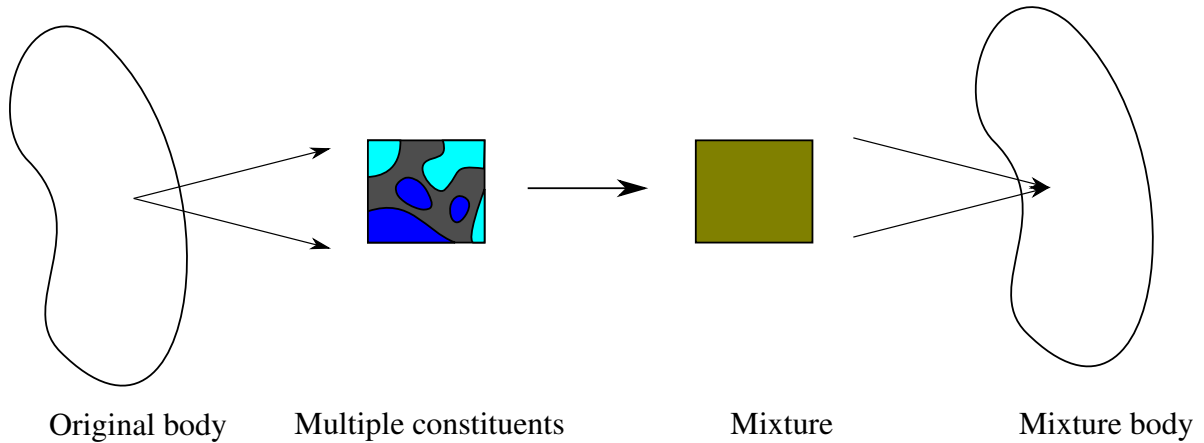
Figure 1.1: Mixture theory

stituent. In most practical cases, only total traction on the boundary of a mixture is known, while mixture theory requires partial traction boundary conditions in its balance laws [41]. This renders the formulation of general initial/boundary-value problems challenging. Another drawback of mixture theory is the absence of the liquid volume fraction as a state variable, which inhibits the modeling of progressive saturation or drying. Mixture theory also requires velocities of all constituents as state variables, which increases the size of computation when implemented numerically.

An alternative approach involves the use of averaging methods, as advocated, e.g., in [28, 30, 29, 7, 45, 46]. Unlike mixture theory, here one introduces the notion of the representative elementary volume (REV), where different parts of the domain are occupied by different phases. Subsequently, the classical balance laws of continuum mechanics are imposed on each phase subject to the requisite interface boundary conditions. Microscopic balance equations are then derived by averaging over the REV. To this end, all macroscopic balance laws are formulated again, while more equations are required to close the system of equation. This approach, while maximally inclusive of the microstructural aspects of the flow, requires an inordinate degree of modeling resolution, and is very challenging for computational implementation.

A purely continuum approach for diffusion through a solid has been developed by Coussy [15, 14, 16], who admits porosity as a state variable and formulates separate balance laws for the pure solid and pure liquid phases. The bulk of Coussy's technical work is predicated on the assumption that the pores of the material are fully saturated. In addition to displacements of the solid and the liquid, liquid volume fraction is introduced as a state variable. Separate mass balance for each phase is formulated by following its own motion. Balance of linear momentum is stipulated for the whole "mixture" system, in which different material time derivatives are used for different phases. To close the system of equations, Coussy also includes constitutive assumptions for liquid diffusion. For unsaturated porous solids [15, Chapter 6], Coussy introduces a saturation variable

for each fluid phase, and formulates mass balance for each phase and linear momentum balance for the whole "mixture" in a similar way as in the saturated case. This approach is also explored in [23, 24, 42, 44], where continuum equations of momentum and energy balance are formulated for the whole "mixture", and are coupled to Darcy's law-based equations for the diffusion of each phase. The crucial assumption posited in this work is that there is an explicitly known functional dependence of the liquid volume fraction on the capillary pressure and the temperature. With this assumption in place, the governing equations become practical and also amenable to finite element modeling.

A lot of effort has been put into the experimental investigation of capillary behavior in porous solids. Leverett's experiment [32, 33] with sand has been widely referenced [13, 9, 52]. In his experiment, Leverett considers a long vertical tube filled with dry sand, in which water is absorbed by the sand through capillary pressure. After several weeks, water distribution reaches a steady state. Water concentration is then measured at each height of the tube. Subsequently an analytical relation is established between capillary pressure and height, since capillary pressure is not directly measurable. Specifically, Leverett proposed a dimensionless function, called the J-function, which relates capillary pressure with liquid saturation, and experimentally studied the form of the J-function for several different types of sand. Leverett concluded that capillary pressure starts with a relatively large value at low liquid saturation, and decreases monotonically to zero as liquid saturation is achieves. In Chapter 4, we will offer a qualitative explanation of the shape of this J-function.

For the driving force of fluid diffusion, there are two main theories, typically associated by Fick's law [21] and Darcy's law [17]. Fick's law relates diffusive flux to the gradient of fluid concentration. It postulates that flow is directed from regions of high concentration to regions of low concentration, with magnitude that is proportional to the concentration gradient. The isotropic form of Fick's law can be mathematically expressed as

$$\mathbf{q} = -D \operatorname{grad} \phi \,, \tag{1.1}$$

where $\mathbf{q}$ is the diffusive flux per unit area per time, D (>0) is the diffusivity constant, and ϕ is the concentration of a fluid. Darcy, on the other hand, proposed a simple proportional relationship between diffusive flow and the fluid pressure gradient, which can be written as

$$\mathbf{q} = -\frac{k}{\mu} \operatorname{grad} p \,, \tag{1.2}$$

where $\mathbf{q}$ is, again, the diffusive flux, k is the permeability of the solid medium, μ is the viscosity of the fluid, and p is the pressure of the fluid. In this work, we will incorporate both theories in our two models. For our single phase liquid diffusion model, with liquid volume fraction as a state variable describing the liquid phase, Fick's law is used. For multiphase diffusion model, which include pressures of gas and liquid phases, Darcy's law is chosen to govern both diffusions.

A minor motivating factor for this thesis is that it has been experimentally observed that high

3
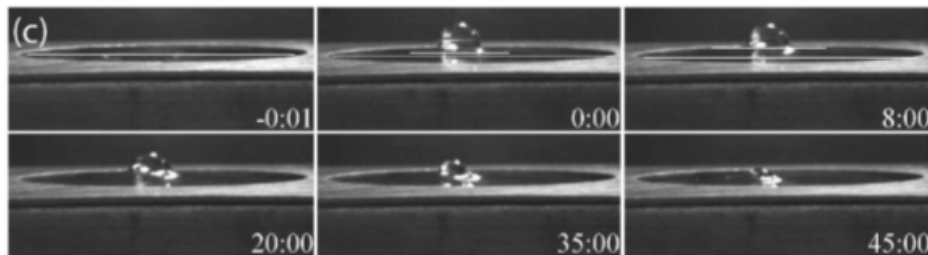
Figure 1.2: Time sequence of water drops on Nafion membrane [27].

water concentration may cause substantial volumetric deformation (swelling) in Nafion® membrane [20, 27], which may, in turn, compromise the integrity of the fuel cell. The swelling of Nafion® has been measured and documented by Benziger [27]. Nafion® membranes bulge almost immediately as a water drop is placed on top of the membrane, and return to flatness as water evaporates. A time sequence of the effect of a water drop on a Nafion® membrane is shown in Figure 1.2.

In this thesis, a new continuum-based theory for the modeling of liquid flow through porous media is proposed and tested using the finite element method. The proposed theory draws from earlier work, but includes several novelties that are specifically intended to broaden its applicability. Specifically, a key assumption here is that the dry solid and the voids are homogenized into a single macroscopic solid medium. This makes sense for materials in which, regardless of the overall porosity, the size of the pores is much smaller that the overall size of the medium. In this case, the liquid phase contributes additively to macroscopic balance laws without need for separate balances for different phases. Moreover, since the balance laws are stated relative to the (homogenized) solid phase, the proposed theory relies on only one set of material time derivatives, namely those relative to the solid frame. Two different approaches will be explored within this framework. First, single phase (liquid) diffusion is modeled, with liquid volume fraction chosen as a state variable and Fick's law as the constitutive assumption. Then, multiphase (liquid and gas) diffusion is modeled, with liquid saturation as a state variable and Darcy's law as the constitutive assumption for diffusion in both phases. In the case of single phase diffusion, a linear relationship between liquid volume fraction and its pressure is proposed as a constitutive assumption. With this assumption, Fick's law coincides with Darcy's law, since the gradient of liquid concentration is proportional to the gradient of liquid pressure. By choosing liquid volume fraction or liquid saturation as a state variable, both models permit the imposition of practical boundary conditions and the precise identification of dry, partially saturated, and fully saturated conditions of the porous medium, as well as the transitions from one such condition to another.

The organization of the thesis is as follows: Chapter 2 contains brief background of continuum mechanics, as required for the presentation of the proposed models. Chapter 3 addresses single phase fluid diffusion in an elastic porous solid, including weak forms of the balance laws required to formulate the finite element approximation. Chapter 4 extends the single phase continuum

4

model by including the gas phase and capillary pressure and by replacing Fick's law with Darcy's law in the constitutive modeling. Chapter 5 documents representative numerical simulations of the single phase and the multiphase models, and further explores the role of gas in multiphase diffusion, as well as the constitutive assumption for capillary pressure. Concluding remarks are offered in Chapter 6.

Chapter 2

Background

2.1 Continuum mechanics

2.1.1 Motion and deformation

Let the continuous solid body $\bar{\mathscr{B}}$ occupy regions $\mathcal{R}_0$ and $\mathcal{R}$ of volume $\mathrm{vol}(\mathcal{R}_0)$ and $\mathrm{vol}(\mathcal{R})$ at times t_0 and t, respectively. These regions have oriented boundaries $\partial\mathcal{R}_0$ and $\partial\mathcal{R}$, which are assumed smooth enough to possess at every point unique outward unit normals $\mathbf{N}$ and $\mathbf{n}$, respectively. Also, let $\mathbf{X}$ be the position vector of a point in $\mathcal{R}_0$ at time t_0. The motion $\boldsymbol{\chi}$ of the continuum maps $\mathbf{X}$ to the vector $\mathbf{x} = \boldsymbol{\chi}(\mathbf{X}, t)$ in $\mathcal{R}$, as in Figure 2.1. The motion is assumed to be invertible for any given time t, and continuously differentiable in both of its arguments. The velocity of a material point occupying $\mathbf{x}$ at time t is subsequently defined as

$$\mathbf{v}(\mathbf{X}, t) = \frac{\partial\boldsymbol{\chi}(\mathbf{X}, t)}{\partial t} \ , \tag{2.1}$$

where $\mathbf{X}$ is the position of the same material point at t_0.

Likewise, the deformation gradient at a point $\mathbf{x}$ in $\mathcal{R}$ relative to its image $\mathbf{X}$ in $\mathcal{R}_0$ is defined as

$$\mathbf{F}(\mathbf{X}, t) = \frac{\partial\boldsymbol{\chi}(\mathbf{X}, t)}{\partial \mathbf{X}} \ . \tag{2.2}$$

An infinitesimal material volume element dV of the reference configuration (associated with the region $\mathcal{R}_0$) is mapped to its image dv (associated with the region $\mathcal{R}$) in the current configuration with the motion $\boldsymbol{\chi}$, and it follows that

$$dv = \det(\mathbf{F})dV \ . \tag{2.3}$$

Since the motion is assumed invertible, $J = \det(\mathbf{F}) \neq 0$ for all $(\mathbf{X}, t)$, and without loss of generality, it is further assumed that $J > 0$.
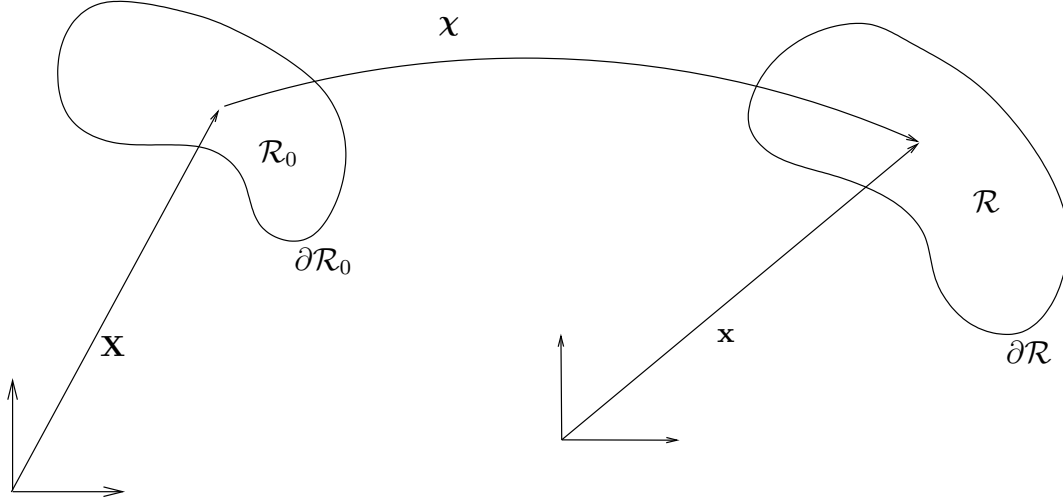
Figure 2.1: Motion of a continuum body

Scalar, vector and tensor functions can be expressed using the Lagrangian description, where the independent variables are the referential position $\mathbf{X}$ and time t, or expressed using the Eulerian description, where the independent variables are the current position $\mathbf{x}$ and time t. For a scalar function ψ, the Lagrangian description can be written as

$$\psi \;=\; \hat{\psi}(\mathbf{X}, t) \,, \tag{2.4}$$

and Eulerian description can be written as

$$\psi \;=\; \tilde{\psi}(\mathbf{x}, t) = \tilde{\psi}(\boldsymbol{\chi}(\mathbf{X}), t) = \hat{\psi}(\mathbf{X}, t) \,. \tag{2.5}$$

The invertibility of the motion guarantees that the Lagrangian and Eulerian description of ψ are equivalent (i.e. each one can be derived from the other).

For a scalar function ψ with Lagrangian description $\psi = \hat{\psi}(\mathbf{X}, t)$, the material time derivative is defined as

$$\dot{\psi} \;=\; \frac{\partial \hat{\psi}(\mathbf{X}, t)}{\partial t} \,. \tag{2.6}$$

Based on the above definition, the material time derivative of ψ is the rate of change of ψ while keeping the referential position $\mathbf{X}$ fixed. For its Eulerian form $\psi = \tilde{\psi}(\mathbf{x}, t)$, the material time derivative is defined as

$$\dot{\psi} \;=\; \frac{\partial \tilde{\psi}(\mathbf{x}, t)}{\partial t} + \operatorname{grad} \tilde{\psi} \cdot \mathbf{v} \,, \tag{2.7}$$

where the first term on the right hand side signifies the change with time of the function at the current position $\mathbf{x}$, and the second term is the convective part of the change of ψ.

7

2.1.2 Classic balance laws

2.1.2.1 Mass conservation

For any material part $\mathcal{P}$ of a body $\mathscr{B}$, its mass should be conserved at any time t, i.e.,

$$\frac{d}{dt} \int_{\mathcal{P}} \rho dv = 0 . \tag{2.8}$$

Using the Reynold's transport theorem, the preceding equation can be written as

$$\int_{\mathcal{P}} (\dot{\rho} + \rho \operatorname{div} \mathbf{v}) dv = 0 . \tag{2.9}$$

Provided that $\mathcal{P}$ is arbitrary, and upon invoking the localization theorem in (2.9), the local form of the mass conservation equation reads,

$$\dot{\rho} + \rho \operatorname{div} \mathbf{v} = 0 . \tag{2.10}$$

2.1.2.2 Linear and angular momentum balance

The linear momentum of any infinitesimal volume element dv in a body can be defined as $\rho \mathbf{v} dv$. We admit the existence of two types of external forces acting on this element, namely body force $\mathbf{b}$ and contact force $\mathbf{t}$. The principle of linear momentum balance states that the rate of change of linear momentum for any region $\mathcal{P}$ at time t equals the total external forces acting on this part, and can be expressed as,

$$\frac{d}{dt} \int_{\mathcal{P}} \rho \mathbf{v} dv = \int_{\mathcal{P}} \rho \mathbf{b} dv + \int_{\partial \mathcal{P}} \mathbf{t} da . \tag{2.11}$$

Taking into account the conservation of mass (2.10), the principle of linear momentum balance can be expressed as

$$\int_{\mathcal{P}} \rho \mathbf{a} \, dv = \int_{\mathcal{P}} \rho \mathbf{b} \, dv + \int_{\partial \mathcal{P}} \mathbf{t} \, da . \tag{2.12}$$

The Cauchy stress tensor $\mathbf{T}$ is defined such that $\mathbf{t}(\mathbf{x}, t, \mathbf{n}) = \mathbf{T}\mathbf{n}$. By substituting this expression for $\mathbf{t}$ in (3.20) with $\mathbf{T}$, and invoking the divergence theorem, linear momentum balance can be written as

$$\int_{\mathcal{P}} \rho \mathbf{a} \, dv = \int_{\mathcal{P}} \rho \mathbf{b} \, dv + \int_{\mathcal{P}} \operatorname{div} \mathbf{T} \, dv . \tag{2.13}$$

Local form of linear momentum balance can be readily expressed in the form

$$\rho \mathbf{a} = \rho \mathbf{b} + \operatorname{div} \mathbf{T} . \tag{2.14}$$

The principle of angular momentum balance states that the rate of change of angular momen-

tum for any region $\mathcal{P}$ occupied at time t equals to the moment of all external forces acting on this part, which is expressed as

$$\frac{d}{dt} \int_{\mathcal{P}} \mathbf{x} \times \rho \mathbf{v} \, dv = \int_{\mathcal{P}} \mathbf{x} \times \rho \mathbf{b} \, dv + \int_{\partial \mathcal{P}} \mathbf{x} \times \mathbf{t}_{(\mathbf{n})} \, da \, . \tag{2.15}$$

Same procedure can be applied to preceding equation, and after invoking linear momentum balance, the above equation can be reduced to

$$\int_{\mathcal{P}} \mathbf{x}_{,i} \times \mathbf{t}_i \, dv = \mathbf{0} \, , \tag{2.16}$$

and local form of angular momentum balance can be written as

$$\mathbf{x}_{,i} \times \mathbf{t}_i = \mathbf{0} \, . \tag{2.17}$$

2.1.3 Invariance

A rigid-body motion is one in which all material particles in the body retain their distance to each other. Now, take a motion $\boldsymbol{\chi}$ of a body $\mathcal{B}$ such that $\mathbf{x} = \boldsymbol{\chi}(\mathbf{X}, t)$, and another motion $\boldsymbol{\chi}^+$ be defined for $\mathcal{B}$ such that $\mathbf{x}^+ = \boldsymbol{\chi}^+(\mathbf{X}, t)$, so that $\boldsymbol{\chi}$ and $\boldsymbol{\chi}^+$ differ only by a rigid body motion. Then, it can be easily established that

$$\mathbf{x}^+ = \mathbf{Q}(t)\mathbf{x} + \mathbf{c}(t) \, , \tag{2.18}$$

where $\mathbf{Q}(t)$ is a time-varying proper orthogonal tensor (i.e. $\mathbf{Q}\mathbf{Q}^T = \mathbf{Q}^T\mathbf{Q} = \mathbf{I}$, $\det \mathbf{Q} = 1$, where $\mathbf{I}$ is the second-order identity tensor), and $\mathbf{c}(t)$ is a vector function of time, which signifies a translation. The transformation of the velocity $\mathbf{v}$ under superposed rigid body motion is as follows

$$\mathbf{v}^+ = \overline{\mathbf{Q}(t)\mathbf{x} + \mathbf{c}(t)} = \dot{\mathbf{Q}}(t)\mathbf{x} + \mathbf{Q}(t)\mathbf{v} + \dot{\mathbf{c}}(t) \, . \tag{2.19}$$

As shown with both the displacement and the velocity, transformation of kinematic terms is governed purely by geometry. However, transformation of kinetic terms and balance laws (both mechanical and thermal) is governed by the principle of invariance under superposed rigid motion. This states that the balance laws should apply regardless of the choice of any superposed rigid motion, hence they should be invariant under superposed rigid motions.

A tensor quantity is called objective if it transforms under superposed rigid body motions in the same manner as its natural basis. A objective scalar ρ transform as

$$\rho^+ = \rho \, . \tag{2.20}$$

An objective referential vector $\mathbf{V}$ and spatial vector $\mathbf{v}$ transform according to

$$\mathbf{V}^+ = \mathbf{V} \, , \quad \mathbf{v}^+ = \mathbf{Q}\mathbf{v} \, . \tag{2.21}$$

Second-order referential tensor $\mathbf{A}$, spatial tensor $\mathbf{B}$, and mixed tensor $\mathbf{F} = F_{iA}\mathbf{e}_i \otimes \mathbf{E}_A$ are similarly objective if they transform as

$$\mathbf{A}^+ = \mathbf{A}, \quad \mathbf{B}^+ = \mathbf{Q}\mathbf{B}\mathbf{Q}^T, \quad \mathbf{F}^+ = \mathbf{Q}\mathbf{F}. \tag{2.22}$$

2.2 Capillarity
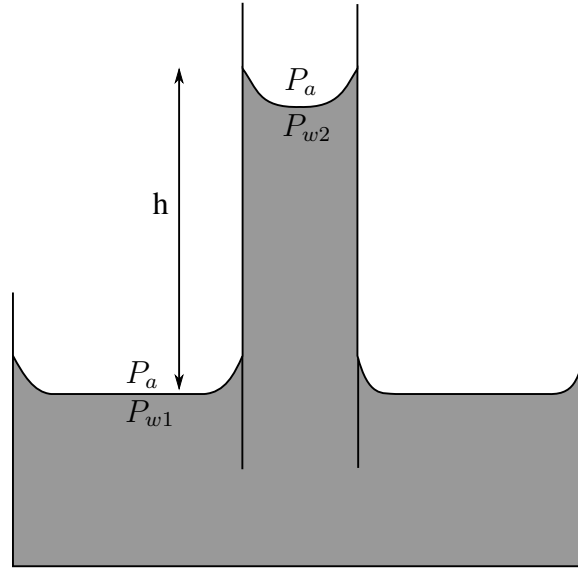
Figure 2.2: Capillary pressure explained in a thin tube

Capillary action is the phenomenon in which liquid ascends through a thin tube or porous media, as shown in Figure 2.2. Capillarity occurs when the intermolecular cohesive force between a liquid is substantially smaller than adhesive force between the liquid molecule and a medium's interacting surface. The difference between adhesive force and cohesive force creates surface tension. The height to which liquid ascends inside a thin tube or porous media is determined by surface tension and size of the tube or the pores.

Capillary pressures are generated where interfaces between two immiscible fluids exist in the pores. Equilibrium at the interface gives the basic relationship between the capillary pressure P_c, the interfacial tension σ, the contact angle θ and the pore radius a as

$$P_c = \frac{2\sigma \cos \theta}{a}. \tag{2.23}$$

In practice, the interfacial tension and the contact angle are impossible to measure. Alternatively, the capillary pressure P_c is estimated by the height of liquid column rises in a thin tube, as

shown in Figure 2.2. Capillary pressure occurs at the top interface between air and water, and

$$P_c = P_{w2} - P_a \ . \tag{2.24}$$

At the surface of the water supply, the pressure of air and water are the same, i.e.

$$P_{w1} \ = \ P_a \ . \tag{2.25}$$

The pressure difference between P_{w1} and P_{w2} is determined by the height of water column in the tube,

$$P_{w2} - P_{w1} = \rho g h \ . \tag{2.26}$$

Combining (2.24),(2.25) and (2.26), the capillary pressure is now expressed as

$$P_c \ = \ \rho g h \ . \tag{2.27}$$

In Chapter 1, we briefly introduced Leverett's experiment which is widely referenced to establish constitutive relation between liquid saturation in porous materials and capillary pressure. In his experiment, a 6 m long vertical tube is filled with dry sand, and water is fed to the bottom of the tube with constant pressure. The top of sand is open to dry air. Water imbibition by capillary pressure through micro channels formed by sands, which is shown in Figure 2.3, takes weeks to reach a steady state.

Leverett measured the liquid concentration at each height in the sand, from which liquid saturation is calculated. Capillary pressure in sand is impossible to measure directly. However, the relationship between capillary pressure and height in micro channels is established in (2.27). Height, which is proportional to capillary pressure, is plotted against liquid saturation for several different types of sand, all of which takes the general qualitative form shown in Figure 2.4. Leverett further proposed a dimensionless function, J-function, and expressed capillary pressure P_c in terms of the J-function of liquid saturation ϕ and a constant σ which has dimension of pressure,

$$P_c \ = \ \sigma J(\phi) \ . \tag{2.28}$$

In this thesis, we will incorporate Leverett's J-function (2.28) in our multiphase diffusion model, in which Darcy's law is used as the governing equation for fluid diffusion through porous solid materials. For a reliable estimate of the J-function, we will start from experiment measurements of capillary pressure and liquid saturation, and introduce a polynomial fit. In addition, we will attempt to justify the form of the J-function by a simple physical argument involving diffusion of liquid through a solid containing an idealized set of microchannels.
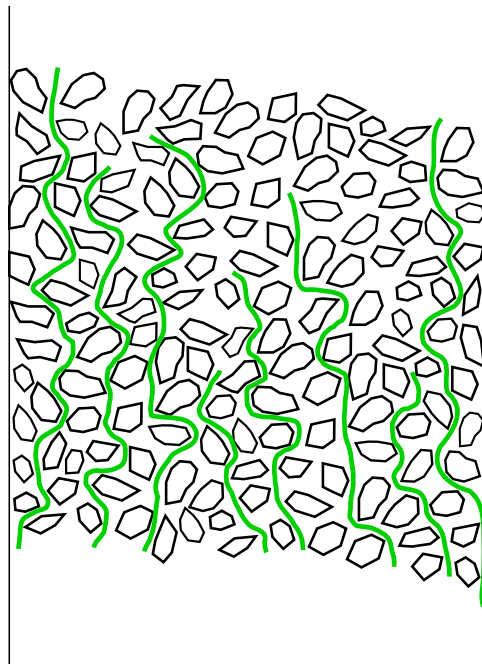
Figure 2.3: Microchannels formed by sand inside the long tube
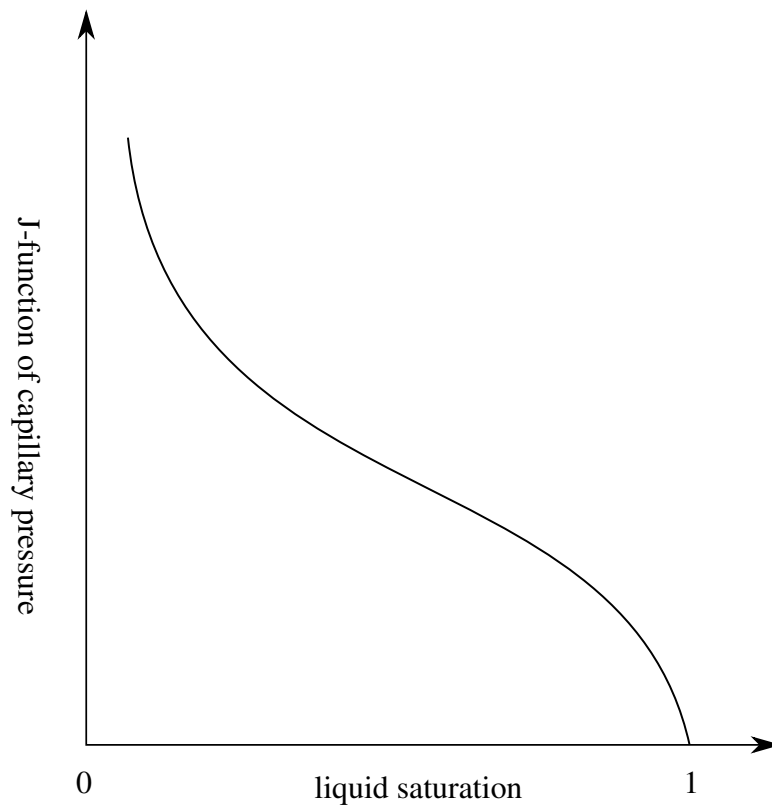
Figure 2.4: Leverett J-function

Chapter 3

Single Phase of Liquid Diffusion in Porous Solid

This chapter concerns liquid diffusion through the voids of a porous solid. The voids and the solid jointly constitute a continuum macroscopic solid phase, which is endowed with a liquid volume fraction to model the liquid phase diffusion. Balance laws are postulated on the macroscopic solid phase, and an initial/boundary-value problem is formulated, a finite element based solution is proposed. Numerical simulations with the model are presented in the Chapter 5.

3.1 Concepts, definitions and constitutive relations

Consider a heterogeneous solid body $\mathscr{B}$ consisting of solid matter and voids (pores) of different sizes and shapes. In this work, it is assumed that the characteristic size of the voids is much smaller than the overall size of the body. Therefore, the material possesses a microstructure consisting of solid and void phases, as shown in Figure 3.1. This microstructure may be locally homogenized to yield a macroscopic continuous solid medium $\bar{\mathscr{B}}$. This medium will be endowed with momentum and density fields, as described below.

3.1.1 Porosity, liquid volume fraction and density

The porosity of a solid is generally defined as the ratio of the volume of voids over the total volume of the porous solid. A local definition of porosity at the macroscale requires the introduction of a representative element of volume $dv \ll \mathrm{vol}(\mathcal{R})$ which accurately resolves the microscopic poral structure of the material. Therefore, the size of dv should be significantly larger than the average size of the pores. Now, the porosity $\bar{\phi}$ of a solid at a macroscopic point may be defined as the ratio of the void volume to the volume dv of the porous solid in the representative element. It follows that, under all circumstances, $0 \le \bar{\phi} < 1$. It is assumed in this work that changes in the porosity $\bar{\phi}$
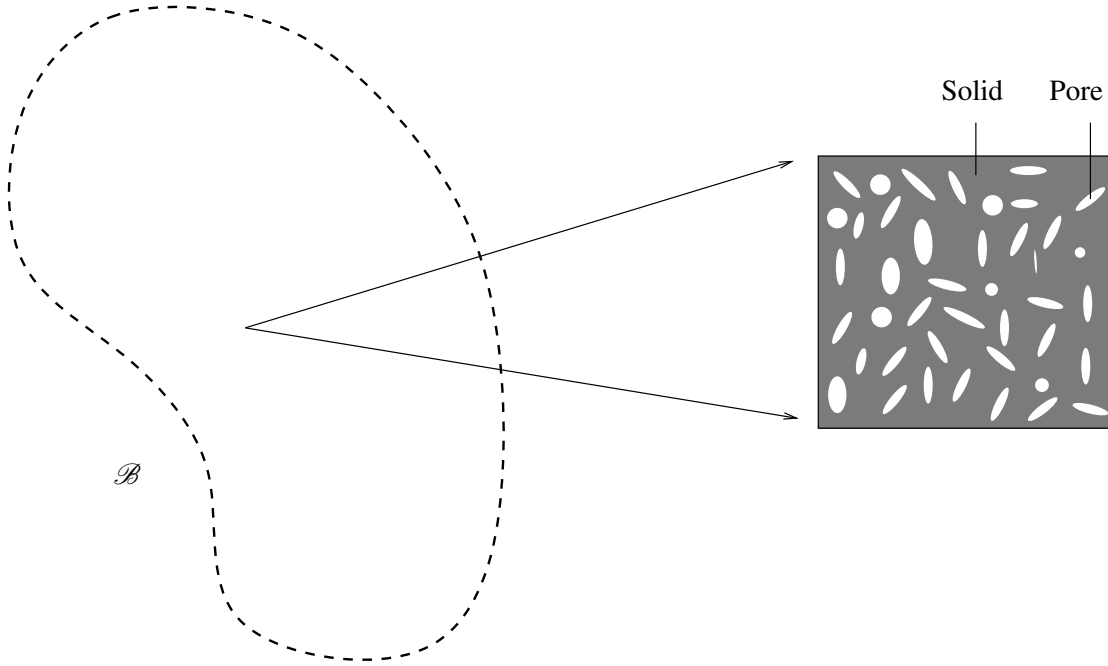
Figure 3.1: Multiscale modeling and homogenization

due to the deformation of the solid are negligible.

Some or all of the pores may be filled with a liquid, rendering the body partially or fully saturated (otherwise, it is referred to as dry). In a partially saturated solid, a fraction of the voids is occupied (either partially or fully) by the liquid, as in Figure 3.2. Specifically, assume that the volume of the liquid in the representative element is dv_l. Now, the liquid volume fraction ϕ is defined locally in the macroscale by

$$dv_l = \phi dv \,, \tag{3.1}$$

where $\phi \leq \bar{\phi}$, with the strict equality holding for the fully saturated case.

Mass conservation in the microscale implies that the macroscopic mass density ρ satisfies the condition

$$\rho dv = \rho_l dv_l + \rho_s dv \,, \tag{3.2}$$

where ρ_l and ρ_s are the densities of the pure liquid and the (dry) porous solid, respectively. Here, ρ_s is a homogenized density which accounts for the presence of voids in the solid.

Equations (3.1) and (3.2) now imply that

$$\rho = \rho_l \phi + \rho_s \,. \tag{3.3}$$

15
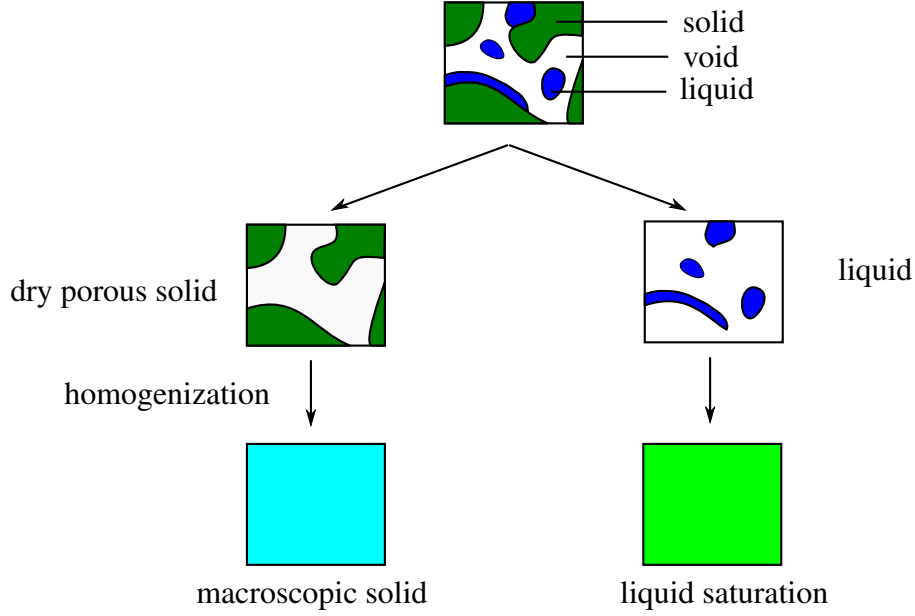
Figure 3.2: Partially saturated porous medium

3.1.2 Liquid mass flux and linear momentum

Preliminary to the definition of liquid mass flux, let $\mathbf{v}_l$ be the velocity of the liquid phase, which, in general, differs from the velocity of the macroscopic solid. Now, the flux of liquid mass through the solid can be expressed as

$$\mathbf{q} \;=\; \rho_l \phi \mathbf{v}^r \,, \tag{3.4}$$

where $\mathbf{v}^r = \mathbf{v}_l - \mathbf{v}$ is the relative velocity of liquid.

Recalling the principal of invariance under superposed rigid motion, note first that both the scalars ρ_l and ϕ are objective. To check objectivity of $\mathbf{v}^r$, let $\mathbf{v}_l$ and $\mathbf{v}$ be the velocities of the liquid and the macroscopic solid at $\mathbf{x}$. Under superposed rigid body motion, $\mathbf{v}_l$ and $\mathbf{v}$ transform according to

$$\mathbf{v}_l^+ = \dot{\mathbf{Q}}(t)\mathbf{x} + \mathbf{Q}(t)\mathbf{v}_l + \dot{\mathbf{c}}(t) \,, \quad \mathbf{v}^+ = \dot{\mathbf{Q}}(t)\mathbf{x} + \mathbf{Q}(t)\mathbf{v} + \dot{\mathbf{c}}(t) \,, \tag{3.5}$$

therefore $\mathbf{v}^r$ transforms according to

$$\mathbf{v}^{r+} \;=\; \mathbf{v}_l^+ - \mathbf{v}^+ \;=\; \mathbf{Q}(t)\mathbf{v}_l - \mathbf{Q}(t)\mathbf{v} \;=\; \mathbf{Q}(t)\mathbf{v}^r \,. \tag{3.6}$$

Combining (3.4) and (3.6), it is easy to show that

$$\mathbf{q}^+ \;=\; \rho^+ \phi^+ \mathbf{v}^{r+} \;=\; \mathbf{Q}(t)\rho\phi\mathbf{v}^r \;=\; \mathbf{Q}(t)\mathbf{q} \,. \tag{3.7}$$

which implies that the flux $\mathbf{q}$ is objective.

Taking into account (3.3) and (3.4), the linear momentum $\rho_s \mathbf{v} + \rho_l \phi \mathbf{v}_l$ of the solid and liquid phases may be written as

$$\rho_s \mathbf{v} + \rho_l \phi \mathbf{v}_l \; = \; \rho \mathbf{v} + \mathbf{q} \,. \tag{3.8}$$

When the material is not fully-saturated, it is assumed that the flux of liquid mass obeys Fick's law [21]. Indeed, this stipulates that the flux of the liquid mass is proportional to the effective liquid density $\rho_l \phi$ and to the gradient of the liquid volume fraction, that is,

$$\mathbf{q} \; = \; -K \rho_l \phi \operatorname{grad} \phi \,, \tag{3.9}$$

where $K(>0)$ is an isotropic diffusivity parameter.

Equations (3.4) and (3.9) permit the representation of the liquid velocity $\mathbf{v}_l$ as a function of the velocity $\mathbf{v}$ of the macroscopic solid and the spatial gradient $\operatorname{grad} \phi$ of the liquid volume fraction according to

$$\mathbf{v}_l \; = \; \mathbf{v} - K \operatorname{grad} \phi \,. \tag{3.10}$$

Therefore, if the densities ρ_s, ρ_l, the velocity $\mathbf{v}$ and the liquid volume fraction ϕ are adopted as state variables in this theory, the preceding observation implies that the liquid velocity $\mathbf{v}_l$ is not an independent state variable. This is an important point of difference from classical mixture theory, as the latter requires the use of velocities for both the solid and the liquid phase.

3.1.3 Effective stress

The macroscopic solid and the liquid contribute to the stress in the body. Here, the cumulative Cauchy stress is assumed to take the form

$$\mathbf{T} \; = \; \mathbf{T}_s - p_l \mathbf{i} \,, \tag{3.11}$$

where $\mathbf{T}_s$ is the stress for the macroscopic solid, p_l is the excess pressure due to the presence of the liquid phase, and $\mathbf{i}$ is the spatial second-order identity tensor. Similar additivity assumptions for stress have been previously utilized in [31, 23, 26]. Both $\mathbf{T}$ and $\mathbf{T}_s$ are assumed to be objective, therefore transform according to $\mathbf{T}^+ = \mathbf{Q}\mathbf{T}\mathbf{Q}^T$ and $\mathbf{T}_s^+ = \mathbf{Q}\mathbf{T}_s\mathbf{Q}^T$.

In this work, the solid response is assumed hyperelastic. For specificity and given the moderate magnitude of the deformation, the solid is taken to obey the Kirchhoff-Saint Venant constitutive law, according to which the second Piola-Kirchhoff stress $\mathbf{S}_s = J\mathbf{F}^{-1}\mathbf{T}_s\mathbf{F}^{-T}$ is given by

$$\mathbf{S}_s \; = \; \lambda \operatorname{tr}(\mathbf{E})\mathbf{I} + 2\mu \mathbf{E} \,. \tag{3.12}$$

Here, $\mathbf{E}$ is the Lagrangian strain, while λ, μ are elastic constants for the macroscopic solid.

The excess pressure due to the liquid phase should clearly depend on the liquid volume fraction,

that is $p_l = \hat{p}_l(\phi)$. For simplicity, a linear relation is assumed here in the form

$$p_l \; = \; C\phi \,, \tag{3.13}$$

where C is a material constant (see [23] for a related assumption).

3.2 Balance laws

Consider a part of the macroscopic solid, which occupies an arbitrary closed and bounded region $\mathcal{P} \subset \mathcal{R}$ with smooth boundary $\partial \mathcal{P}$ at time t.

   Balance of mass and linear momentum are formulated below by examining the material in region $\mathcal{P}$. Here, all material time derivatives of integrals over $\mathcal{P}$ are defined by keeping material particles of the macroscopic solid fixed.

3.2.1 Balance of mass

The rate of change of total mass for the region $\mathcal{P}$ occupied by the macroscopic solid at time t takes the form

$$\frac{d}{dt} \int_{\mathcal{P}} \rho \, dv \; = \; \frac{d}{dt} \int_{\mathcal{P}} \rho_s \, dv + \frac{d}{dt} \int_{\mathcal{P}} \rho_l \phi \, dv \,, \tag{3.14}$$

where use is made of (3.3). Since the mass of the macroscopic solid material is conserved, the preceding equation readily reduces to

$$\frac{d}{dt} \int_{\mathcal{P}} \rho \, dv \; = \; \frac{d}{dt} \int_{\mathcal{P}} \rho_l \phi \, dv \,. \tag{3.15}$$

This is contrasted to the conventional mass balance statement in (2.8). Also, since all changes of the liquid mass in $\mathcal{P}$ are due to the flux of the liquid $\mathbf{q}$ at the boundary $\partial \mathcal{P}$, it follows from (3.15) that the balance of total mass may be expressed simply as

$$\frac{d}{dt} \int_{\mathcal{P}} \rho_l \phi \, dv \; = \; - \int_{\partial \mathcal{P}} \mathbf{q} \cdot \mathbf{n} \, da \,. \tag{3.16}$$

   Appealing to the Reynolds' transport, divergence and localization theorems, the integral statement (3.16) gives rise to a corresponding local statement, which is given by

$$\frac{d}{dt}(\rho_l \phi) + \rho_l \phi \, \mathrm{div} \, \mathbf{v} \; = \; - \, \mathrm{div} \, \mathbf{q} \,. \tag{3.17}$$

Alternatively, combining (3.15) and (3.16), mass balance may be expressed in term of the macro-

scopic mass density as

$$\dot{\rho} + \rho \operatorname{div} \mathbf{v} = -\operatorname{div} \mathbf{q} . \tag{3.18}$$

Again, the local form of mass balance is contrasted to the conventional form (2.10) to appreciate the effect of the liquid flux $\mathbf{q}$. Also, in comparing equation (3.18) to the corresponding mass balance equation in classical mixture theory, it is noted that the latter is obtained by summing the respective balance equations for the different phases and defining an equivalent material time derivative as a linear combination of the density-weighted derivatives of the individual phases. Clearly, no such summation is needed here, because the mass balance equation is written with respect to the macroscopic solid and, hence, incorporates changes to the fluid mass through the flux term $\mathbf{q}$.

The conventional local form of mass balance is recovered from (3.18) by merely setting $\mathbf{q} = \mathbf{0}$.

3.2.2 Balance of linear momentum

Balance of linear momentum necessitates that the rate of change of total linear momentum for the region $\mathcal{P}$ occupied by the macroscopic solid at time t be equal to the external forces acting on the material and the flux of linear momentum $-(\rho_l \phi \mathbf{v}_l) \mathbf{v}^r \cdot \mathbf{n}$ through the boundary $\partial \mathcal{P}$. This translates to

$$\frac{d}{dt} \int_{\mathcal{P}} (\rho_s \mathbf{v} + \rho_l \phi \mathbf{v}_l) \, dv = \int_{\mathcal{P}} \rho \mathbf{b} \, dv + \int_{\partial \mathcal{P}} \mathbf{t} \, da - \int_{\partial \mathcal{P}} (\rho_l \phi \mathbf{v}_l) \mathbf{v}^r \cdot \mathbf{n} \, da , \tag{3.19}$$

where $\mathbf{t} = \mathbf{T} \mathbf{n}$ is the traction vector on $\partial \mathcal{P}$. Recalling (3.4) and (3.8), the preceding equation may be equivalently rewritten as

$$\frac{d}{dt} \int_{\mathcal{P}} (\rho \mathbf{v} + \mathbf{q}) \, dv = \int_{\mathcal{P}} \rho \mathbf{b} \, dv + \int_{\partial \mathcal{P}} \mathbf{t} \, da - \int_{\partial \mathcal{P}} (\mathbf{q} \cdot \mathbf{n}) \mathbf{v}_l \, da . \tag{3.20}$$

Invoking, again, the Reynolds' transport theorem and also the mass balance equation (3.18) and the divergence theorem, the integral statement of linear momentum (3.20) may be recast in the form

$$\int_{\mathcal{P}} \left(\rho \frac{d\mathbf{v}}{dt} - \mathbf{v} \operatorname{div} \mathbf{q} + \frac{d\mathbf{q}}{dt} + \mathbf{q} \operatorname{div} \mathbf{v} \right) dv = \int_{\mathcal{P}} \rho \mathbf{b} \, dv + \int_{\mathcal{P}} \operatorname{div} \mathbf{T} \, dv - \int_{\mathcal{P}} \operatorname{div} (\mathbf{v}_l \otimes \mathbf{q}) \, dv . \tag{3.21}$$

The corresponding local form follows readily from (3.21), and reads

$$\rho \frac{d\mathbf{v}}{dt} - \mathbf{v} \operatorname{div} \mathbf{q} + \frac{d\mathbf{q}}{dt} + \mathbf{q} \operatorname{div} \mathbf{v} = \rho \mathbf{b} + \operatorname{div} \mathbf{T} - \operatorname{div} (\mathbf{v}_l \otimes \mathbf{q}) . \tag{3.22}$$

Again, setting $\mathbf{q} = \mathbf{0}$ reduces (3.22) to the conventional local form of linear momentum balance.

3.3 Finite element implementation

3.3.1 Weak forms

In this section, weak counterparts of the local balance equations (3.17) and (3.22) are constructed preliminary to finite element discretization.

For mass balance, equation (3.17) is first weighted by a scalar test function η, then integrated over $\mathcal{P}$, so that, upon invoking integration by parts and the divergence theorem, it leads to

$$\int_{\mathcal{P}} \eta \rho_l \frac{d\phi}{dt} \, dv + \int_{\mathcal{P}} \eta \rho_l \phi \operatorname{div} \mathbf{v} \, dv - \int_{\mathcal{P}} \operatorname{grad} \eta \cdot \mathbf{q} dv + \int_{\partial \mathcal{P}} \eta \mathbf{q} \cdot \mathbf{n} \, da \;=\; 0 \,. \tag{3.23}$$

Likewise, for balance of linear momentum, equation (3.22) is contracted with an arbitrary vector test function $\boldsymbol{\xi}$ and integrated over the domain $\mathcal{P}$. This leads to

$$\int_{\mathcal{P}} \boldsymbol{\xi} \cdot \rho \frac{d\mathbf{v}}{dt} \, dv - \int_{\mathcal{P}} \boldsymbol{\xi} \cdot \mathbf{v} \operatorname{div} \mathbf{q} \, dv + \int_{\mathcal{P}} \boldsymbol{\xi} \cdot \frac{d\mathbf{q}}{dt} \, dv + \int_{\mathcal{P}} \boldsymbol{\xi} \cdot \mathbf{q} \operatorname{div} \mathbf{v} \, dv - \int_{\mathcal{P}} \boldsymbol{\xi} \cdot \rho \mathbf{b} \, dv$$
$$- \int_{\mathcal{P}} \boldsymbol{\xi} \cdot \operatorname{div} \mathbf{T} \, dv + \int_{\mathcal{P}} \boldsymbol{\xi} \cdot \mathbf{v}_l \operatorname{div} \mathbf{q} \, dv + \int_{\mathcal{P}} \boldsymbol{\xi} \cdot \big[(\operatorname{grad} \mathbf{v}_l) \mathbf{q} \big] \, dv \;=\; 0 \,. \tag{3.24}$$

Applying integration by parts and the divergence theorem to the second and sixth terms on the left-hand side of (3.24), one may recast the preceding weak form as

$$\int_{\mathcal{P}} \boldsymbol{\xi} \cdot \rho \frac{d\mathbf{v}}{dt} \, dv + \int_{\mathcal{P}} \big[(\operatorname{grad} \boldsymbol{\xi}) \mathbf{q} \big] \cdot \mathbf{v} \, dv + \int_{\mathcal{P}} \boldsymbol{\xi} \cdot \big[(\operatorname{grad} \mathbf{v}) \mathbf{q} \big] \, dv - \int_{\partial \mathcal{P}} \big[(\boldsymbol{\xi} \cdot \mathbf{v}) \mathbf{q} \big] \cdot \mathbf{n} \, da$$
$$+ \int_{\mathcal{P}} \boldsymbol{\xi} \cdot \frac{d\mathbf{q}}{dt} \, dv + \int_{\mathcal{P}} \boldsymbol{\xi} \cdot \mathbf{q} \operatorname{div} \mathbf{v} \, dv - \int_{\mathcal{P}} \boldsymbol{\xi} \cdot \rho \mathbf{b} \, dv + \int_{\mathcal{P}} \operatorname{grad} \boldsymbol{\xi} \cdot \mathbf{T} dv - \int_{\partial \mathcal{P}} \boldsymbol{\xi} \cdot \mathbf{t} \, da$$
$$+ \int_{\mathcal{P}} \boldsymbol{\xi} \cdot \mathbf{v}_l \operatorname{div} \mathbf{q} \, dv + \int_{\mathcal{P}} \boldsymbol{\xi} \cdot \big[(\operatorname{grad} \mathbf{v}_l) \mathbf{q} \big] \, dv \;=\; 0 \,. \tag{3.25}$$

The last two terms on the left-hand side of (3.25) may be further rewritten with the aid of integration by parts and the divergence theorem as

$$\int_{\mathcal{P}} \boldsymbol{\xi} \cdot \mathbf{v}_l \operatorname{div} \mathbf{q} \, dv + \int_{\mathcal{P}} \boldsymbol{\xi} \cdot \big[(\operatorname{grad} \mathbf{v}_l) \mathbf{q} \big] \, dv \;=\; \int_{\partial \mathcal{P}} \big[(\boldsymbol{\xi} \cdot \mathbf{v}_l) \mathbf{q} \big] \cdot \mathbf{n} \, da - \int_{\mathcal{P}} \big[(\operatorname{grad} \boldsymbol{\xi}) \mathbf{q} \big] \cdot \mathbf{v}_l \, dv \,. \tag{3.26}$$

This leads to an alternative expression for the weak form of linear momentum balance as

$$\int_{\mathcal{P}} \boldsymbol{\xi} \cdot \rho \frac{d\mathbf{v}}{dt}\, dv + \int_{\mathcal{P}} \left[(\operatorname{grad} \boldsymbol{\xi}) \mathbf{q} \right] \cdot (K \operatorname{grad} \phi)\, dv + \int_{\mathcal{P}} \boldsymbol{\xi} \cdot \left[(\operatorname{grad} \mathbf{v}) \mathbf{q} \right]\, dv$$

$$+ \int_{\mathcal{P}} \boldsymbol{\xi} \cdot \frac{d\mathbf{q}}{dt}\, dv + \int_{\mathcal{P}} \boldsymbol{\xi} \cdot \mathbf{q} \operatorname{div} \mathbf{v}\, dv - \int_{\mathcal{P}} \boldsymbol{\xi} \cdot \rho \mathbf{b}\, dv + \int_{\mathcal{P}} \operatorname{grad} \boldsymbol{\xi} \cdot \mathbf{T}\, dv$$

$$- \int_{\partial\mathcal{P}} \boldsymbol{\xi} \cdot \mathbf{t}\, da - \int_{\partial\mathcal{P}} \left[(\boldsymbol{\xi} \cdot (K \operatorname{grad} \phi)) \mathbf{q} \right] \cdot \mathbf{n}\, da \ = \ 0\,, \quad (3.27)$$

where the liquid velocity is eliminated by using (3.10).

3.3.2 Space and time discretization

In the finite element setting, the domain of the continuum macroscopic porous solid body is approximated by a set $\boldsymbol{\Omega}$ of nonoverlapping elements such that $\mathcal{R} \approx \boldsymbol{\Omega} = \bigcup_{I=1}^{n_{elmt}} \boldsymbol{\Omega}^{I}$, where n_{elmt} is number of elements. The macroscopic solid displacement $\mathbf{u}$ and liquid volume fraction ϕ, as well as test functions $\boldsymbol{\xi}$ and η are approximated by nodal interpolations as

$$\mathbf{u}(\mathbf{x}, t) = \sum_{I=1}^{N_{node}} N_I(\mathbf{x}) \hat{\mathbf{u}}_I(t)\,, \qquad\qquad \phi(\mathbf{x}, t) = \sum_{I=1}^{N_{node}} N_I(\mathbf{x}) \hat{\phi}_I(t)$$

$$\boldsymbol{\xi}(\mathbf{x}, t) = \sum_{J=1}^{N_{node}} N_J(\mathbf{x}) \hat{\boldsymbol{\xi}}_J(t)\,, \qquad\qquad \eta(\mathbf{x}, t) = \sum_{J=1}^{N_{node}} N_J(\mathbf{x}) \hat{\eta}_J(t)\,. \qquad (3.28)$$

Here, n_{node} is the number of nodes in an element, $N_I(\mathbf{x})$ is the shape function at node I, $\hat{\mathbf{u}}_I(t)$, $\hat{\phi}_I(t)$, are the nodal values of the solid displacement and liquid volume fraction at node I and time t, and $\hat{\boldsymbol{\xi}}_I(t)$, $\hat{\eta}_I(t)$ are corresponding nodal values of test function $\boldsymbol{\xi}$ and η at node I and time t.

Substitute the spatial interpolation (3.28) in mass balance equation (3.23), The indicial form of its residual at I node becomes

$$\hat{\eta}_I \left[\int_{\mathcal{P}} N_I \rho_l \dot{\phi}\, dv + \int_{\mathcal{P}} N_I \rho_l \phi \operatorname{div} \mathbf{v}\, dv - \int_{\mathcal{P}} N_{I,m} q_m dv + \int_{\partial\mathcal{P}} N_I q_m n_m\, da \right] \ = \ 0\,. \qquad (3.29)$$

The arbitrariness of the testing function β implies that the residual force R_I vanishes, that is

$$R_I \ = \ \int_{\mathcal{P}} N_I \rho_l \dot{\phi}\, dv + \int_{\mathcal{P}} N_I \rho_l \phi \operatorname{div} \mathbf{v}\, dv - \int_{\mathcal{P}} N_{I,m} q_m dv + \int_{\partial\mathcal{P}} N_I q_m n_m\, da \ = \ 0\,. \qquad (3.30)$$

Same procedure is applied to linear momentum (3.27), the indicial form of its residual at the

I^{th} node becomes

$$
\hat{\xi}_{Ii} \Big[\int_{\mathcal{P}} N_I \rho a_j \delta_{ij}\, dv + \int_{\mathcal{P}} N_{I,m} q_n K \phi_{,j} \delta_{mn} \delta_{ij}\, dv + \int_{\mathcal{P}} N_I v_{j,m} q_n \delta_{ij} \delta_{mn}\, dv
$$

$$
+ \int_{\mathcal{P}} N_I \frac{dq_j}{dt} \delta_{ij}\, dv + \int_{\mathcal{P}} N_I q_j \delta_{ij}\, \mathrm{div}\, \mathbf{v}\, dv - \int_{\mathcal{P}} N_I \rho b_j \delta_{ij}\, dv + \int_{\mathcal{P}} N_{I,m} T_{jm} \delta_{ij} \delta_{mn}\, dv
$$

$$
- \int_{\partial \mathcal{P}} N_I t_j \delta_{ij}\, da - \int_{\partial \mathcal{P}} K N_I \phi_{,j} q_n n_m \delta_{ij} \delta_{mn}\, da \Big] = 0\,, \quad (3.31)
$$

where i, j, m, n are spatial coordinate indices.

Again, the arbitrariness of the testing function $\boldsymbol{\xi}$ implies that the residual force R_{Ii} vanishes, that is

$$
R_{Ii} = \int_{\mathcal{P}} N_I \rho a_j \delta_{ij}\, dv + \int_{\mathcal{P}} N_{I,m} q_n K \phi_{,j} \delta_{mn} \delta_{ij}\, dv + \int_{\mathcal{P}} N_I v_{j,m} q_n \delta_{ij} \delta_{mn}\, dv
$$

$$
+ \int_{\mathcal{P}} N_I \frac{dq_j}{dt} \delta_{ij}\, dv + \int_{\mathcal{P}} N_I q_j \delta_{ij}\, \mathrm{div}\, \mathbf{v}\, dv - \int_{\mathcal{P}} N_I \rho b_j \delta_{ij}\, dv + \int_{\mathcal{P}} N_{I,m} T_{jm} \delta_{ij} \delta_{mn}\, dv
$$

$$
- \int_{\partial \mathcal{P}} N_I t_j \delta_{ij}\, da - \int_{\partial \mathcal{P}} K N_I \phi_{,j} q_n n_m \delta_{ij} \delta_{mn}\, da = 0\,. \quad (3.32)
$$

The final assembled residual equation can be written as a nonlinear function of the displacement $\mathbf{u}$, the velocity $\mathbf{v}$, the acceleration $\mathbf{a}$, the liquid volume fraction ϕ, and the time derivative of liquid volume fraction $\dot{\phi}$, as

$$
\mathbf{R}(\mathbf{u}, \mathbf{v}, \mathbf{a}, \phi, \dot{\phi}) = \mathbf{0}\,. \quad (3.33)
$$

To solve the coupled system of first- and second-order ordinary differential equations in time, a one-step time integration algorithm is introduced. In a typical time interval $(t_n, t_{n+1}]$ by using an implicit Newmark scheme [36], such that

$$
\begin{aligned}
\mathbf{u}_{n+1} &= \mathbf{u}_n + \mathbf{v}_n \Delta t_n + \frac{1}{2} \left[(1 - 2\beta) \mathbf{a}_n + 2\beta \mathbf{a}_{n+1} \right] \Delta t_n^2 \\
\mathbf{v}_{n+1} &= \mathbf{v}_n + \left[(1 - \gamma) \mathbf{a}_n + \gamma \mathbf{a}_{n+1} \right] \Delta t_n \\
\phi_{n+1} &= \phi_n + \left[(1 - \gamma) \dot{\phi}_n + \gamma \dot{\phi}_{n+1} \right] \Delta t_n\,,
\end{aligned} \quad (3.34)
$$

where $(\cdot)_n = (\cdot) \mid_n = (\cdot)(t_n)$, $\Delta t_n = t_{n+1} - t_n$, and $\beta \in (0, 1/2]$, $\gamma \in (0, 1]$ are the Newmark parameters. The typical choice for the latter is $\beta = 1/4$, $\gamma = 1/2$, which compares to the classical trapezoidal rule.

A Newton-Raphson method is adopted to solve the nonlinear algebraic equation $\mathbf{R}_i = 0$ re-

sulting from the application of (3.34) to (3.33). This can be written in component form as

$$R_i^{(k+1)} = R_i^{(k)} + \frac{\partial R_i}{\partial \alpha_j}\bigg|^{(k)} d\alpha_j^{(k)} = 0 \;, \tag{3.35}$$

where α_j is one of the variables at time t_{n+1}, and k is the iteration number for the Newton-Raphson method. Stiffness matrix for solving equation (3.33) is defined as

$$K_{ij}^{(k)} = -\frac{\partial R_i}{\partial \alpha_j}\bigg|^{(k)} \tag{3.36}$$

Since the residual function R can be expressed with the aid of (3.34) only in terms of $\mathbf{u}$ and ϕ, the stiffness matrix is written as

$$K_{ij}\Delta u_j = -\frac{\partial R_i}{\partial u_j}\Delta u_j - \frac{\partial R_i}{\partial v_k}\frac{\partial v_k}{\partial u_j}\Delta u_j - \frac{\partial R_i}{\partial a_k}\frac{\partial a_k}{\partial u_j}\Delta u_j \;, \tag{3.37}$$

and

$$K_{ij}\Delta \phi_j = -\frac{\partial R_i}{\partial \phi_j}\Delta \phi_j - \frac{\partial R_i}{\partial \dot{\phi}_k}\frac{\partial \dot{\phi}_k}{\partial \phi_j}\Delta \phi_j \;, \tag{3.38}$$

where Δu_j, $\Delta \phi_j$ are increments of the unknown variables.

Newmark formulas (3.34) give

$$\frac{\partial v_k}{\partial u_j} = \frac{\gamma}{\beta \Delta t}\delta_{kj} \;, \quad \frac{\partial a_k}{\partial u_j} = \frac{1}{\beta \Delta t^2}\delta_{kj} \;, \tag{3.39}$$

and

$$\frac{\partial \dot{\phi}_k}{\partial \phi_j} = \frac{1}{\gamma \Delta t}\delta_{kj} \;. \tag{3.40}$$

Stiffness matrix $\mathbf{K}$ can be readily calculated as following,

$$K_{ij}\Delta u_j = -\frac{\partial R_i}{\partial u_j}\Delta u_j - \frac{\gamma}{\beta \Delta t}\frac{\partial R_i}{\partial v_k}\Delta u_j - \frac{1}{\beta \Delta t^2}\frac{\partial R_i}{\partial a_k}\Delta u_j \;, \tag{3.41}$$

and

$$K_{ij}\Delta \phi_j = -\frac{\partial R_i}{\partial \phi_j}\Delta \phi_j - \frac{1}{\gamma \Delta t}\frac{\partial R_i}{\partial \dot{\phi}_k}\Delta \phi_j \;. \tag{3.42}$$

The detailed consistent linearization of the residual R weak forms with respect to $\mathbf{u}$ and ϕ is derived in the Appendix A.

Chapter 4

Multiphase Diffusion in Porous Solid

This chapter expands the modeling capability to include multiphase flow. With the same continuum macroscopic solid phase, porosity is again viewed as a local material property. To model liquid diffusion in the presence of a gas phase, capillary pressure is included in the expanded model. After forming the balance laws on the macroscopic solid, and setting the initial/boundary-value problem, a finite element solution is again developed, and numerical simulations are discussed in Chapter 5.

4.1 Definitions

4.1.1 General definitions

Consider a porous body $\mathcal{B}$ consisting of solid matter and voids of different sizes and shapes. When the body is dry, all the pores are occupied by gas (typically, air). Otherwise, the pores may be either partially or fully occupied by liquid matter, as shown in Figure 4.1.

Next, assume, again, that the characteristic size of the voids be much smaller than the overall size of the body. Now, the porous solid can be locally homogenized to yield a macroscopic continuous solid endowed with a density field ρ_s. This homogenization altogether excludes the liquid and gas phases.

The bulk porosity ϵ ($0 \leq \epsilon \leq 1$) may now be defined at any point of the macroscopic solid as the ratio of the volume of voids to the volume of the macroscopic solid in a representative element $\mathcal{V}$ centered at the point. Such a definition is meaningful provided that the porosity field is well-defined for a representative element volume which is much smaller than the total volume of the body, that is, if $\mathrm{vol}(\mathcal{V}) \ll \mathrm{vol}(\mathcal{R})$.

The preceding homogenization procedure may be employed to also define the saturation ϕ at a point as the ratio of the volume of liquid to the volume of the void in the representative element volume. Therefore, $\phi = 0$ corresponds to dry pores and $\phi = 1$ to fully saturated ones. In the partially saturated case ($0 < \phi < 1$), gas occupies any portion on the pores that is not filled with
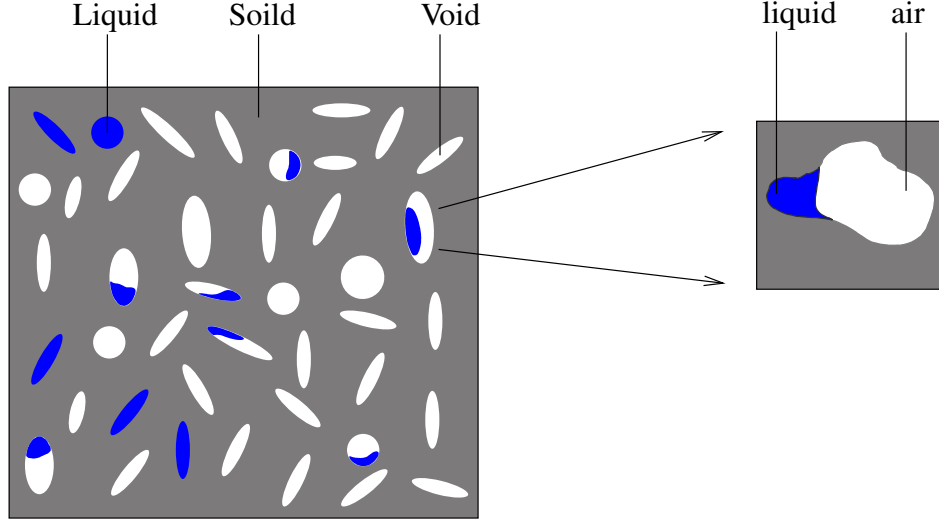
Figure 4.1: Partially saturated porous solid

liquid. Therefore, the total density ρ of the porous medium is

$$\rho \;=\; \rho_s + \rho_l \epsilon \phi + \rho_g \epsilon (1 - \phi)\,, \tag{4.1}$$

where ρ_l and ρ_g are densities of the liquid and gas phases. Both densities are taken to be constant: for the liquid, this is an immediate implication of homogeneity and incompressibility, while for the gas it is due to the assumption that the gas is allowed to move freely through the pores without being subject to compression.

The diffusion of liquid and gas matter in the porous medium is characterized by the fluxes of liquid $\mathbf{q}_l$ and gas $\mathbf{q}_g$ in the macroscopic solid, defined as

$$\mathbf{q}_l \;=\; \rho_l \epsilon \phi \mathbf{v}_l^r \quad , \quad \mathbf{q}_g \;=\; \rho_g \epsilon (1 - \phi) \mathbf{v}_g^r\,. \tag{4.2}$$

Here, $\mathbf{v}_l^r$ and $\mathbf{v}_g^r$ are the liquid and gas velocities relative to the macroscopic solid. These are related to the respective absolute velocities $\mathbf{v}_l$ and $\mathbf{v}_g$ as $\mathbf{v}_l^r = \mathbf{v}_l - \mathbf{v}$ and $\mathbf{v}_g^r = \mathbf{v}_g - \mathbf{v}$. Repeating again the argument in Section 3.1.2, it is easy to conclude that the two fluxes are objective.

4.2 Balance laws

Consider a part of the macroscopic solid, which occupies an arbitrary closed and bounded region $\mathcal{P} \subset \mathcal{R}$ with smooth boundary $\partial \mathcal{P}$ having outward normal $\mathbf{n}$ at time t.

Balance of mass and linear momentum are formulated below by examining the material in region $\mathcal{P}$. Here, all material time derivatives of integrals over $\mathcal{P}$ are defined by keeping material

particles of the macroscopic solid fixed.

4.2.1 Balances of mass

Since all balance laws are formulated on a material domain $\mathcal{P}$ relative to the macroscopic solid material, mass conservation for the macroscopic solid is automatically satisfied. Additional mass balance laws are required for the liquid and gas phases.

For the liquid phase, the rate of change of mass equals the flux of liquid leaving the domain from the boundary $\partial \mathcal{P}$, hence it takes the form

$$\frac{d}{dt} \int_{\mathcal{P}} \rho_l \epsilon \phi \, dv \; = \; - \int_{\partial \mathcal{P}} \mathbf{q}_l \cdot \mathbf{n} \, da \; . \tag{4.3}$$

Upon using the Reynolds' transport theorem and the divergence theorem, the local form of (4.3) is derived as

$$\frac{d(\rho_l \epsilon \phi)}{dt} + \rho_l \epsilon \phi \, \mathrm{div}\, \mathbf{v} \; = \; - \,\mathrm{div}\, \mathbf{q}_l \; . \tag{4.4}$$

Likewise, the mass balance for the gas phase is written in integral form as

$$\frac{d}{dt} \int_{\mathcal{P}} \rho_g \epsilon (1 - \phi) \, dv \; = \; - \int_{\partial \mathcal{P}} \mathbf{q}_g \cdot \mathbf{n} \, da \; , \tag{4.5}$$

with its local counterpart expressed as

$$\frac{d\big(\rho_g \epsilon (1 - \phi)\big)}{dt} + \rho_g \epsilon (1 - \phi) \, \mathrm{div}\, \mathbf{v} \; = \; - \,\mathrm{div}\, \mathbf{q}_g \; . \tag{4.6}$$

4.2.2 Balance of linear momentum

The proposed theory relies on a single linear momentum balance law, rather than on individual balances for each phase. This circumvents the need to resolve all force interactions between the constituent phases.

The rate of change of the total linear momentum is equal to the total external force acting on the material and the flux of linear momentum of the liquid and gas phases. This means that the integral statement of linear momentum balance for the domain $\mathcal{P}$ is given as

$$\frac{d}{dt} \int_{\mathcal{P}} (\rho_s \mathbf{v} + \rho_l \epsilon \phi \mathbf{v}_l + \rho_g \epsilon (1 - \phi) \mathbf{v}_g) \, dv \; =$$
$$\int_{\mathcal{P}} \rho \mathbf{b} \, dv + \int_{\partial \mathcal{P}} \mathbf{t} \, da - \int_{\partial \mathcal{P}} (\mathbf{q}_l \cdot \mathbf{n}) \mathbf{v}_l \, da - \int_{\partial \mathcal{P}} (\mathbf{q}_g \cdot \mathbf{n}) \mathbf{v}_g \, da \; . \tag{4.7}$$

Taking into account (4.1) and (4.2), the left-hand side of (4.7) may be rewritten as

$$\frac{d}{dt} \int_{\mathcal{P}} \left(\rho_s \mathbf{v} + \rho_l \epsilon \phi \mathbf{v}_l + \rho_g \epsilon (1 - \phi) \mathbf{v}_g \right) dv = \frac{d}{dt} \int_{\mathcal{P}} (\rho \mathbf{v} + \mathbf{q}_l + \mathbf{q}_g) \, dv . \tag{4.8}$$

Using the mass balance equations (4.4) and (4.6) and the Reynolds' transport theorem, the right-hand side of the above equation becomes

$$\frac{d}{dt} \int_{\mathcal{P}} (\rho \mathbf{v} + \mathbf{q}_l + \mathbf{q}_g) \, dv =$$
$$\int_{\mathcal{P}} \left(\rho \frac{d\mathbf{v}}{dt} - \mathbf{v}(\operatorname{div} \mathbf{q}_g + \operatorname{div} \mathbf{q}_l) + \frac{d\mathbf{q}_g}{dt} + \mathbf{q}_g \operatorname{div} \mathbf{v} + \frac{d\mathbf{q}_l}{dt} + \mathbf{q}_l \operatorname{div} \mathbf{v} \right) dv . \tag{4.9}$$

Combining (4.9) and (4.7) and invoking the divergence theorem, the local form of the linear momentum balance equation is deduced in the form

$$\rho \frac{d\mathbf{v}}{dt} - \mathbf{v}(\operatorname{div} \mathbf{q}_g + \operatorname{div} \mathbf{q}_l) + \frac{d\mathbf{q}_g}{dt} + \mathbf{q}_g \operatorname{div} \mathbf{v} + \frac{d\mathbf{q}_l}{dt} + \mathbf{q}_l \operatorname{div} \mathbf{v} =$$
$$\rho \mathbf{b} + \operatorname{div} \mathbf{T} - \operatorname{div} \mathbf{q}_g \mathbf{v}_g - (\operatorname{grad} \mathbf{v}_g)\mathbf{q}_g - \operatorname{div} \mathbf{q}_l \mathbf{v}_l - (\operatorname{grad} \mathbf{v}_l)\mathbf{q}_l , \tag{4.10}$$

where $\mathbf{T}$ is the Cauchy stress of the body.

4.3   Constitutive assumptions

The balance laws furnish a total of five equations, two from mass and three from linear momentum balance to determine twelve unknowns, that is the macroscopic solid displacement $\mathbf{u}$, the liquid saturation ϕ, the liquid pressure p_l, the gas pressure p_g, the relative liquid velocity $\mathbf{v}_l^r$ and the relative gas velocity $\mathbf{v}_g^r$. Therefore, closure of the system necessitates the introduction of seven constitutive equations.

The diffusion of liquid and gas matter in the macroscopic solid is assumed to be governed by Darcy's law, which states that diffusion is driven by (and is proportional to) the gradient of pressure. Therefore, the constitutive assumptions for the relative velocities of liquid and gas take the form

$$\mathbf{v}_l^r = -\frac{k_l}{\mu_l} \operatorname{grad} P_l \quad , \quad \mathbf{v}_g^r = -\frac{k_g}{\mu_g} \operatorname{grad} P_g , \tag{4.11}$$

where k_l, k_g, μ_l, and μ_g are liquid and gas permeabilities and viscosities, respectively.

The final equation needed to close the system concerns the capillary pressure, which is the difference in pressure across the interface between gas and liquid in equilibrium, that is

$$P_c = P_l - P_g . \tag{4.12}$$

Leverett [33] introduced a dimensionless function $J(\phi)$ to which the capillary pressure P_c is assumed to be proportional, that is

$$P_c \ = \ \sigma J(\phi) \, , \tag{4.13}$$

where σ is a constant that has the dimension of pressure. Several analytical expressions of the Leverett J-function have been proposed in the literature for different applications, see, e.g., [12, 25, 51].

Here, we offer a qualitative argument for the overall form of the J-function. One may consider porous media as comprising many microchannels formed by pores. Liquid may diffuse through such microchannels as in the idealized porous medium whose cross-section is locally characterized by the regular structure of the representative area element depicted in Figure 4.2. Denoting the

(a) Dry

(b) Low saturation

(c) High saturation

(d) Full saturation
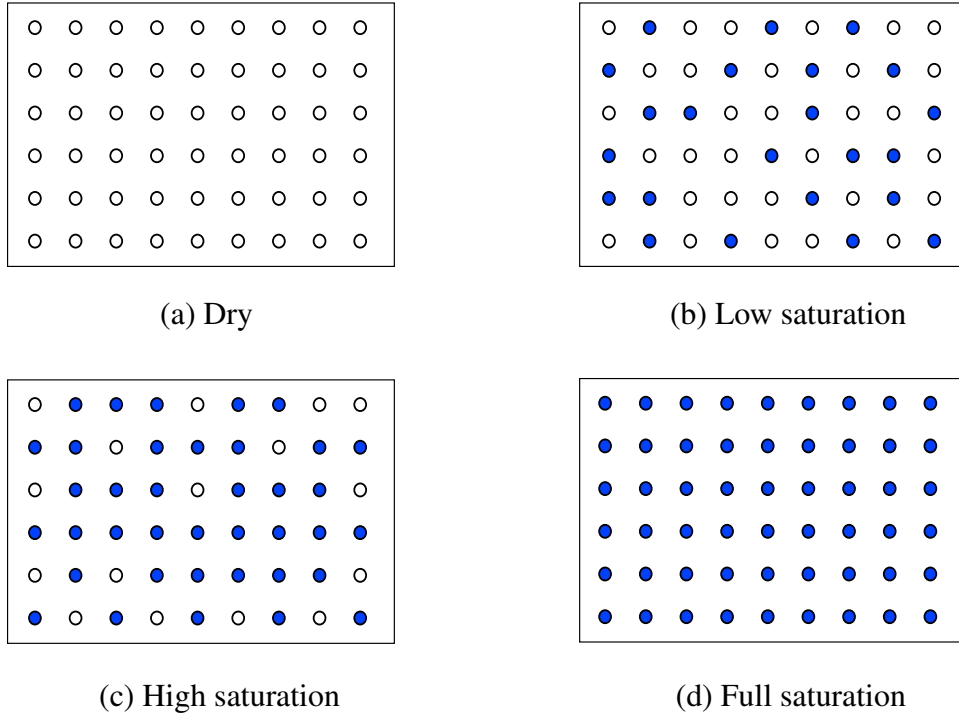
Figure 4.2: Local structure of the representative area element of an idealized porous medium at four different states of saturation ("wet" microchannels are shown as filled blue circles and "dry" ones are shown as unfilled circle)

(average) capillary pressure in a non-saturated microchannels p_c° and letting the (average) cross-section of a microchannel be A°, the local homogenized capillary pressure P_c is

$$P_c \ = \ \frac{N p_c^\circ A^\circ}{A} \, , \tag{4.14}$$

where N is total number of non-saturated microchannels and A is the total area of the representative

area element of the cross-section. When the porous medium is essentially dry as in Figure 4.2a, (that is, ϕ approaches zero), all the microchannels are non-saturated, therefore N is large, which yields a high capillary pressure P_c. As the medium gets progressively more saturated with liquid (hence, ϕ increases), as in Figure 4.2b,c, N decreases, and so does the capillary pressure P_c. In the limiting case of full saturation ($\phi = 1$) depicted in Figure 4.2d, N approaches zero, as does P_c. In conclusion, the preceding argument implies that the J-function is monotonically decreasing to zero with increasing values of ϕ. While the argument suggests linearity of J in N, this does not necessarily translate to linearity of J in ϕ, since the geometric structure of the microchannels is far more complex than that of straight parallel tubes assumed here.

Here, we further explore the nonlinearity of the J-function first by relating area saturation and the volume saturation. By definition, area saturation ϕ_{area} is the ratio of the area of saturated microchannels to the total area, so $\frac{NA^\circ}{A}$ in (4.14) is equal to $1 - \phi_{area}$, and this equation implies

$$P_c \; \propto \; 1 - \phi_{area} \; . \tag{4.15}$$

It is reasonable to assume that microchannels in different orientations are saturated at the same pace, so volume saturation ϕ and area saturation ϕ_{area} follow a simple relation as below

$$\phi \; = \; \phi_{area}^{\frac{3}{2}} \; . \tag{4.16}$$

The two preceding equations give us a nonlinear relation between the J-function and ϕ, which is plotted in Figure 4.3.

Next, we consider nonlinearity of the J-function caused by the statistical distribution of the areas of microchannels. Let the areas of the microchannels follow a random distribution, and recall that capillary pressure of each microchannel is a function of the radius of the microchannel, as given in (2.23). Also, let the microchannel with higher capillary pressure be saturated before the ones with lower capillary pressure. For the cases where the areas of the microchannels follow a normal distribution or a uniform distribution, the J-function takes nonlinear forms as illustrated again in Figure 4.3. Therefore, in summary, the capillary pressure decreases as the porous medium is saturated progressively, and the J-function takes a nonlinear form which is caused by the geometry of the microchannels in the porous medium and the randomness in the pore sizes.

In this thesis, we assume that the J-function depends polynomially on ϕ where all polynomial coefficients have the dimension of pressure and are obtained by curve-fitting of experimental measurements of the capillary pressure for different values of liquid saturation. In particular, a simple cubic polynomial approximation is considered in the form

$$P_c \; = \; c_1\phi^3 + c_2\phi^2 + c_3\phi + c_4 \; , \tag{4.17}$$

where the coefficients c_i, $i = 1 - 4$, are determined for each porous medium from experimental data [39, 8, 19]. It will be shown in Section 5.2 that this approximation captures with accuracy the
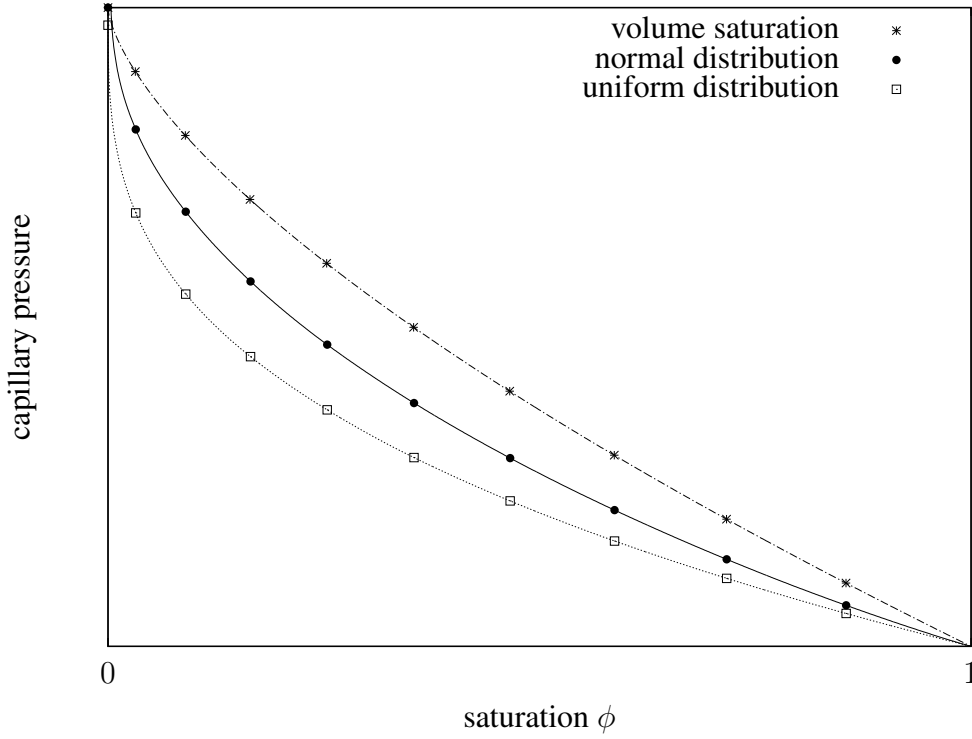
Figure 4.3: Nonlinear J-function explained by saturation and random distribution of areas of the microchannels

salient features of the dependency of P_c on ϕ for different types of porous media.

The macroscopic solid, gas and liquid phases contribute to the homogenized stress in the body, and the cumulative Cauchy stress is assumed to be in the form

$$\mathbf{T} = \mathbf{T}_s - (P_l + P_g)\mathbf{i} \tag{4.18}$$

where $\mathbf{T}_s$ is the stress for the macroscopic solid, and $\mathbf{i}$ is spatial second-order identity tensor.

A special case of the theory arises when the capillary pressure is assumed to be linear in ϕ, according to

$$P_c = \sigma(1 - \phi) . \tag{4.19}$$

It follows, upon recalling (4.2), (4.11), and (4.12), that the liquid mass flux is reduced to

$$\mathbf{q}_l = -\rho_l \epsilon \phi \frac{k_l}{\mu_l} (\operatorname{grad} P_g - \sigma \operatorname{grad} \phi) . \tag{4.20}$$

In addition, if the gas pressure is taken to be uniform inside the porous medium, the equation for

liquid flux is further reduced to be

$$\mathbf{q}_l = K_d \rho_l \epsilon \phi \operatorname{grad} \phi \,, \tag{4.21}$$

where liquid diffusivity constant K_d is given by $\frac{k_l \sigma}{\mu_l}$. This equation now coincides to the one derived in an earlier work [54]. Also, gas mass flux is zero through out the porous medium in this case due to uniform gas pressure, therefore mass balance for gas is automatically satisfied.

4.4 Finite element approximation

4.4.1 Weak forms

In this section, weak forms of the local balance equations (4.4), (4.6) and (4.10) are constructed by way of background to the finite element approximation. element time and space discretization.

For liquid and gas mass balance, equations (4.4) and (4.6) are first weighted by arbitrary scalar test functions η and ζ, then integrated over $\mathcal{P}$. After using integration by parts and invoking the divergence theorem, the weak forms of liquid and gas mass balance become

$$\int_{\mathcal{P}} \eta \rho_l \epsilon \frac{d\phi}{dt}\, dv + \int_{\mathcal{P}} \eta \rho_l \epsilon \phi \operatorname{div} \mathbf{v}\, dv - \int_{\mathcal{P}} \operatorname{grad} \eta \cdot \mathbf{q}_l\, dv + \int_{\partial \mathcal{P}} \eta \mathbf{q}_l \cdot \mathbf{n}\, da = 0 \tag{4.22}$$

and

$$\int_{\mathcal{P}} \zeta \rho_g \epsilon \frac{d(1-\phi)}{dt}\, dv + \int_{\mathcal{P}} \zeta \rho_g \epsilon (1-\phi) \operatorname{div} \mathbf{v}\, dv - \int_{\mathcal{P}} \operatorname{grad} \zeta \cdot \mathbf{q}_g\, dv + \int_{\partial \mathcal{P}} \zeta \mathbf{q}_g \cdot \mathbf{n}\, da = 0\,, \tag{4.23}$$

respectively.

Likewise for linear momentum balance, equation (4.10) is first weighted by an arbitrary vector test function ξ, and integrated over $\mathcal{P}$. Again, after the straightforward application of integration by parts and the divergence theorem, the weak form of linear momentum balance is expressed as

$$\int_{\mathcal{P}} \boldsymbol{\xi} \cdot \rho \frac{d\mathbf{v}}{dt}\, dv - \int_{\partial \mathcal{P}} \left[(\boldsymbol{\xi} \cdot \mathbf{v}) \mathbf{q}_g \right] \cdot \mathbf{n}\, da + \int_{\mathcal{P}} \left[(\operatorname{grad} \boldsymbol{\xi}) \mathbf{q}_g \right] \cdot \mathbf{v}\, dv + \int_{\mathcal{P}} \boldsymbol{\xi} \cdot \left[(\operatorname{grad} \mathbf{v}) \mathbf{q}_g \right] dv$$

$$+ \int_{\mathcal{P}} \boldsymbol{\xi} \cdot \frac{d\mathbf{q}_g}{dt}\, dv + \int_{\mathcal{P}} \boldsymbol{\xi} \cdot \mathbf{q}_g \operatorname{div} \mathbf{v}\, dv - \int_{\partial \mathcal{P}} \left[(\boldsymbol{\xi} \cdot \mathbf{v}) \mathbf{q}_l \right] \cdot \mathbf{n}\, da + \int_{\mathcal{P}} \left[(\operatorname{grad} \boldsymbol{\xi}) \mathbf{q}_l \right] \cdot \mathbf{v}\, dv + \int_{\mathcal{P}} \boldsymbol{\xi} \cdot \left[(\operatorname{grad} \mathbf{v}) \mathbf{q}_l \right] dv$$

$$+ \int_{\mathcal{P}} \boldsymbol{\xi} \cdot \frac{d\mathbf{q}_l}{dt}\, dv + \int_{\mathcal{P}} \boldsymbol{\xi} \cdot \mathbf{q}_l \operatorname{div} \mathbf{v}\, dv - \int_{\mathcal{P}} \boldsymbol{\xi} \cdot \rho \mathbf{b}\, dv + \int_{\mathcal{P}} \operatorname{grad} \boldsymbol{\xi} \cdot \mathbf{T}\, dv - \int_{\partial \mathcal{P}} \boldsymbol{\xi} \cdot \mathbf{t}\, da + \int_{\partial \mathcal{P}} \left[(\boldsymbol{\xi} \cdot \mathbf{v}_g) \mathbf{q}_g \right] \cdot \mathbf{n}\, da$$

$$- \int_{\mathcal{P}} \left[(\operatorname{grad} \boldsymbol{\xi}) \mathbf{q}_g \right] \cdot \mathbf{v}_g\, dv + \int_{\partial \mathcal{P}} \left[(\boldsymbol{\xi} \cdot \mathbf{v}_l) \mathbf{q}_l \right] \cdot \mathbf{n}\, da - \int_{\mathcal{P}} \left[(\operatorname{grad} \boldsymbol{\xi}) \mathbf{q}_l \right] \cdot \mathbf{v}_l\, dv = 0\,. \tag{4.24}$$

The preceding equation may be simplified by combining the second and third term with the fif-

teenth and sixteenth term, and also the seventh and eighth with the seventeenth and eighteenth term, leading to

$$
\int_{\mathcal{P}} \boldsymbol{\xi} \cdot \rho \frac{d\mathbf{v}}{dt} \, dv + \int_{\partial\mathcal{P}} \left[(\boldsymbol{\xi} \cdot \mathbf{v}_g^r) \mathbf{q}_g \right] \cdot \mathbf{n} \, da - \int_{\mathcal{P}} \left[(\operatorname{grad} \boldsymbol{\xi}) \mathbf{q}_g \right] \cdot \mathbf{v}_g^r \, dv + \int_{\mathcal{P}} \boldsymbol{\xi} \cdot \left[(\operatorname{grad} \mathbf{v}) \mathbf{q}_g \right] \, dv
$$
$$
+ \int_{\mathcal{P}} \boldsymbol{\xi} \cdot \frac{d\mathbf{q}_g}{dt} \, dv + \int_{\mathcal{P}} \boldsymbol{\xi} \cdot \mathbf{q}_g \operatorname{div} \mathbf{v} \, dv + \int_{\partial\mathcal{P}} \left[(\boldsymbol{\xi} \cdot \mathbf{v}_l^r) \mathbf{q}_l \right] \cdot \mathbf{n} \, da - \int_{\mathcal{P}} \left[(\operatorname{grad} \boldsymbol{\xi}) \mathbf{q}_l \right] \cdot \mathbf{v}_l^r \, dv
$$
$$
+ \int_{\mathcal{P}} \boldsymbol{\xi} \cdot \left[(\operatorname{grad} \mathbf{v}) \mathbf{q}_l \right] \, dv + \int_{\mathcal{P}} \boldsymbol{\xi} \cdot \frac{d\mathbf{q}_l}{dt} \, dv + \int_{\mathcal{P}} \boldsymbol{\xi} \cdot \mathbf{q}_l \operatorname{div} \mathbf{v} \, dv - \int_{\mathcal{P}} \boldsymbol{\xi} \cdot \rho \mathbf{b} \, dv + \int_{\mathcal{P}} \operatorname{grad} \boldsymbol{\xi} \cdot \mathbf{T} \, dv - \int_{\partial\mathcal{P}} \boldsymbol{\xi} \cdot \mathbf{t} \, da \; = \; 0 \, .
$$

$$(4.25)$$

4.4.2 Space and time discretization

A finite element approximation is effected on the weak forms (4.22), (4.23) and (4.25). Owing to the arbitrariness of the test functions η, ζ and $\boldsymbol{\xi}$, the weak forms give rise to a coupled system of integro-differential equations with the macroscopic solid displacement $\mathbf{u}$, liquid saturation ϕ and gas pressure p_g as unknown variables.

Following standard procedure, semi-discretization is employed for the solution of (4.22), (4.23) and (4.25) with displacement-like finite element approximation used for the spatial discretization of $\mathbf{u}$, ϕ and P_g, similar to the procedure showed in Section 3.3.2. This results in a coupled system of first- and second-order ordinary partial differential equations in time. These, in turn, are integrated in a typical time interval $(t_n, t_{n+1}]$ using an implicit Newmark method [36], according to which

$$
\begin{aligned}
\mathbf{u}_{n+1} &= \mathbf{u}_n + \mathbf{v}_n \Delta t_n + \frac{1}{2} \left[(1 - 2\beta) \mathbf{a}_n + 2\beta \mathbf{a}_{n+1} \right] \Delta t_n^2 \, , \\
\mathbf{v}_{n+1} &= \mathbf{v}_n + \left[(1 - \gamma) \mathbf{a}_n + \gamma \mathbf{a}_{n+1} \right] \Delta t_n \, , \\
\phi_{n+1} &= \phi_n + \left[(1 - \gamma) \dot{\phi}_n + \gamma \dot{\phi}_{n+1} \right] \Delta t_n \, , \\
P_{g,n+1} &= P_{g,n} + \left[(1 - \gamma) \dot{P}_{g_n} + \gamma \dot{P}_{g_{n+1}} \right] \Delta t_n \, .
\end{aligned}
$$

$$(4.26)$$

The resulting nonlinear algebraic equations are solved at any discrete time t_{n+1} with the Newton-Raphson method. This requires consistent linearization of the weak forms with respect to $\mathbf{u}$, ϕ and P_g, which is derived in the Appendix.

Chapter 5

Numerical Simulations

5.1 Single Phase Liquid Diffusion in Porous Solid

The finite element formulation of the model described in Chapter 3. was implemented in the general-purpose nonlinear program FEAP, which is partially documented in [49, 48]. The model and its numerical implementation were tested on three representative simulations discussed below. All simulations employed 8-node isoparametric brick elements with full $2 \times 2 \times 2$ Gaussian quadrature. In addition, the time integration parameters defined in Section 3.3.2 were set to $\beta = 0.25$ and $\gamma = 0.5$.

The material properties in the simulations were chosen for Nafion[®], which is suitable for modeling within the proposed theory, owing to the small size of its pores (with diameter of 20–30 nm [22]) compared to the typical thickness of industrial Nafion[®] membranes (0.175 mm [34]). The Nafion[®] properties were set to: $(\lambda, \mu) = (0.40 \times 10^7, 0.27 \times 10^7) \, \mathrm{Pa}$ [43], $\rho_s = 2 \times 10^3 \, \mathrm{kgr/m^3}$ [43], $\rho_l = 10^3 \, \mathrm{kgr/m^3}$, $\bar{\phi} = 0.4$ [47], $K = 1.0 \times 10^{-10} \, \mathrm{m^2/s}$ [35], and $C = 10^6 \, \mathrm{Pa}$. The last parameter was chosen heuristically such that the liquid excess pressure p_l in (3.13) be in the range of one atmosphere at saturation.

5.1.1 Stretching of a saturated cube

A $0.5 \, \mathrm{mm}$ cube made of saturated Nafion[®] is stretched uniformly using displacement control on one face while being fixed on the opposite face and free on all four lateral faces. Zero liquid flux boundary conditions are enforced on the whole boundary. The imposed stretching is applied at time $t = 0$ and the body is subsequently allowed to reach steady-state.

A uniform $10 \times 5 \times 5$ mesh is used to discretize the domain, with the finer resolution aligned with the direction of stretching (here, the x-direction). Also, time integration is performed with constant step-size $\Delta t = 10^{-6} \, \mathrm{s}$.

Figure 5.1 shows the distribution of the liquid volume fraction along the centerline of the cube in the x-direction at three different times and for stretch $\lambda = 0.1$. At $t = 10^{-6} \, \mathrm{s}$, the body is
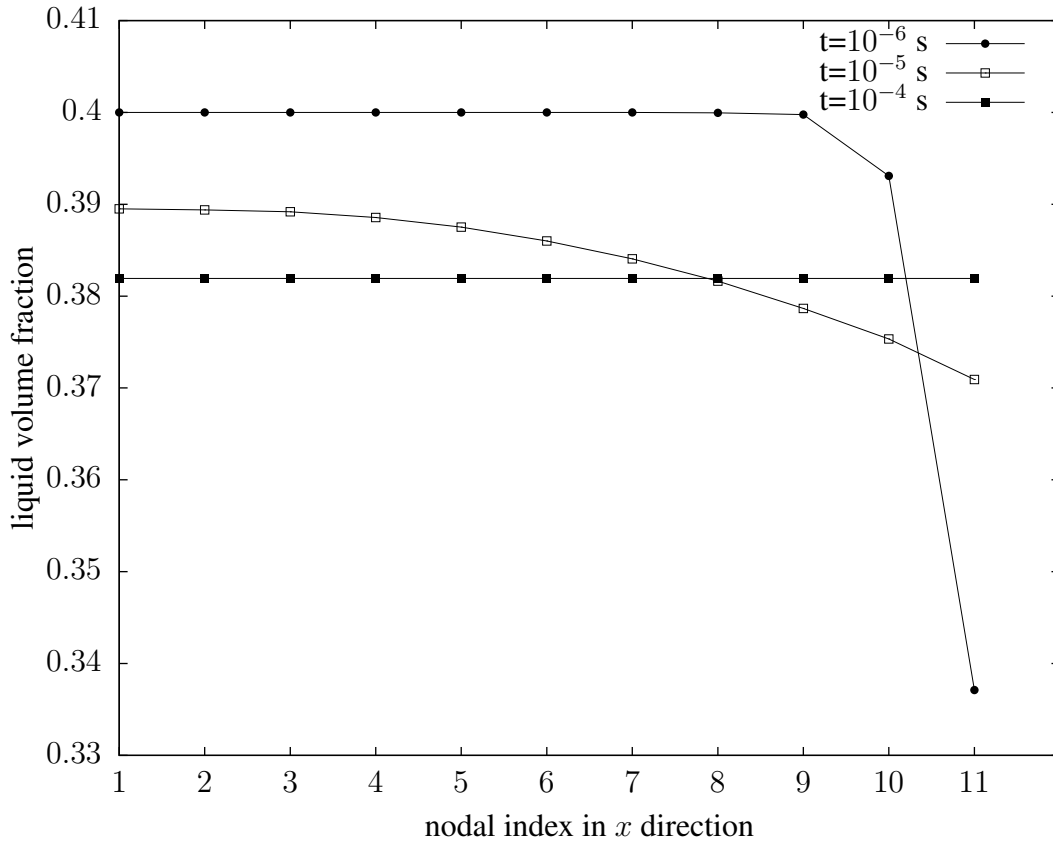
Figure 5.1: Stretching of a saturated cube: Liquid volume fraction at the nodes along the centerline of the stretch direction at different times (nodes are indexed from 1 to 11 with the latter being on the stretched side)

essentially saturated away from the stretched end, while near this end its liquid volume fraction exhibits a precipitous drop. At $t = 10^{-5}$ s, the distribution of the liquid volume fraction is much smoother reflecting the flow of liquid toward the stretched end of the body, while at $t = 10^{-4}$ s the volume fraction is spatially uniform and below the saturation limit due to the attainment of steady-state.

Next, the cube is stretched in increments of $\Delta\lambda = 0.1$ up to a total stretch of $\lambda = 0.4$. After each stretch increment, the body is allowed to reach steady-state before the next increment is imposed. The relation between the liquid volume fraction at steady-state and the stretch is illustrated in Figure 5.2 and shows the expected monotonic decrease. The same figure also depicts the total volume of the liquid, which remains constant throughout the stretch loading owing to the zero-flux boundary conditions.
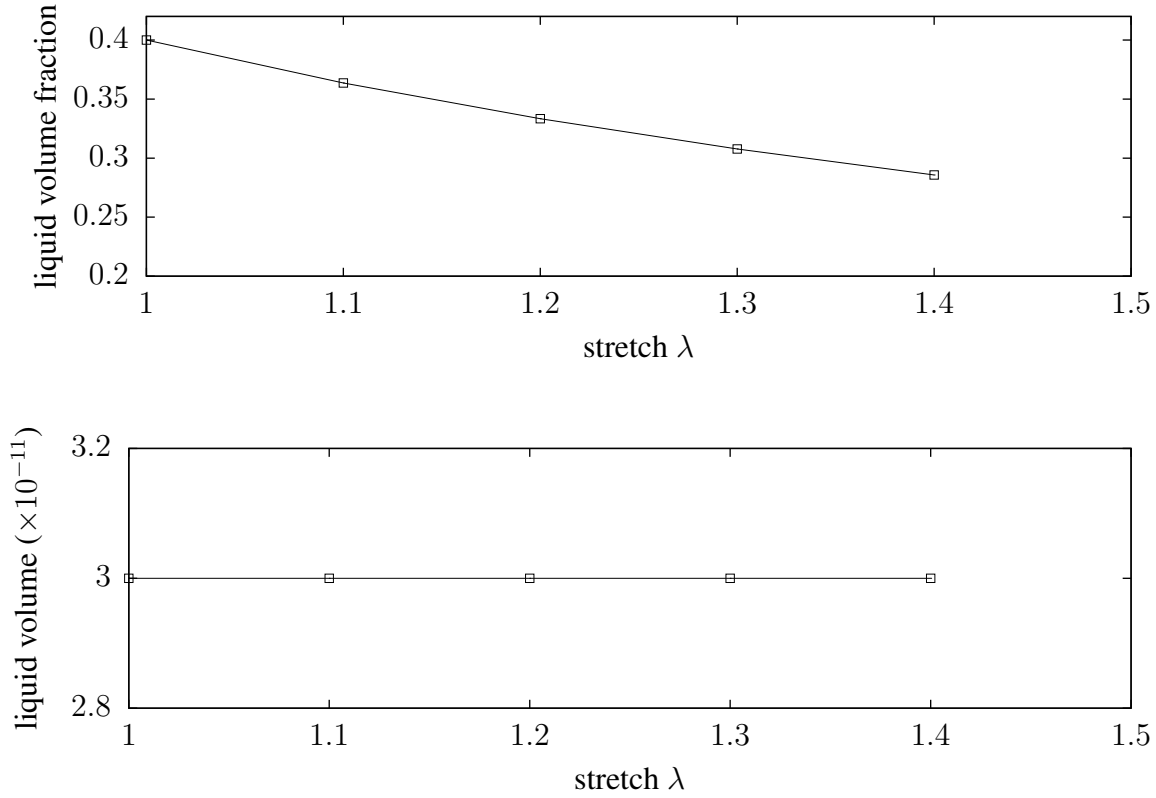
Figure 5.2: Stretching of a saturated cube: Liquid volume fraction at steady-state as a function of stretch (top) and conservation of liquid volume (bottom)

5.1.2 Squeezing of a saturated cube

A 0.5 mm cube of saturated Nafion$^{\circledR}$ is compressed uniformly on one of its faces using displacement control, while the opposite face remains fixed and each of the four lateral faces is free to slide on its own plane only. The liquid may escape from the compressed face, while all other faces are assumed to be impermeable. The block is initially squeezed to $\lambda_s = 93\%$ while keeping the liquid volume fraction to the saturation value of $\phi = 0.4$ on the compressed face. Then, it is stretched back to its original shape, where it is kept until the liquid volume fraction reaches steady state. During the stretching and until steady state is attained, the compressed face is subject to zero liquid flux conditions. Each of the three loading stages is imposed proportionally over a period of 0.1 s.

A uniform $5 \times 5 \times 5$ mesh is used in this problem and the time step-size is set to $\Delta t = 1$ ms. As illustrated in Figure 5.3, the total volume of the liquid decreases during squeezing, then remains constant while the body returns to its original configuration. At the same time, the total volume of

the porous medium initially decreases and then increases back to its original value.
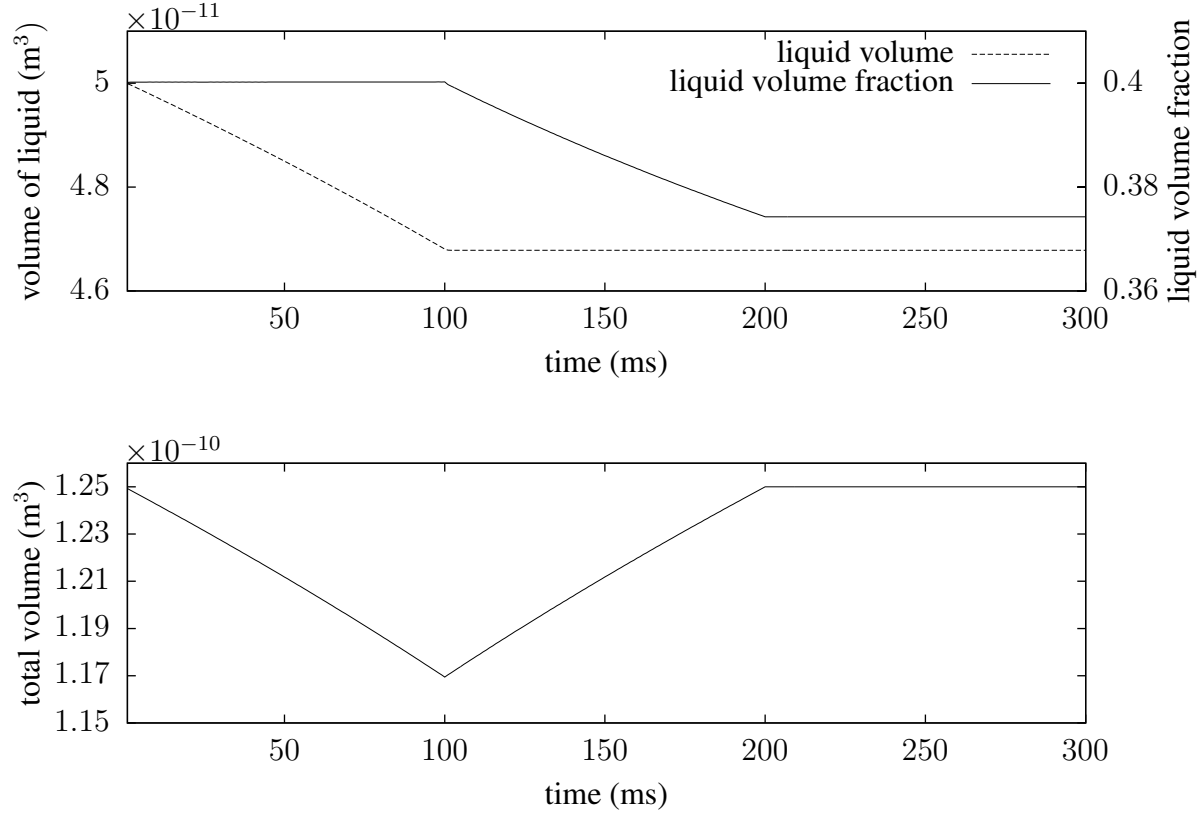
Figure 5.3: Squeezing of a saturated cube: Liquid and total volume as a function of time

The same block is subsequently subjected to repeated squeezing and stretching of the same magnitude and rate as before. In this case, liquid escapes from the solid block repeatedly until the solid material pushes enough of it out of the block to reach a steady state of liquid volume fraction. To prevent back-flow into the block, the fixed liquid volume fraction boundary condition on the compressed face during squeezing is chosen to be equal to the minimum of the current steady-state liquid volume fraction and the asymptotic liquid volume fraction ϕ_a at maximum squeezing. The latter is equal, in this case, to

$$\phi_a = \frac{\lambda_s V - (1 - \bar{\phi})V}{\lambda_s V} = \frac{0.93 - (1 - 0.4)}{0.93} \doteq 0.35 \,, \tag{5.1}$$

where V denotes the initial volume of the block. The preceding definition is predicated upon the assumption that the solid matter (being hyperelastic) returns to its original volume when the liquid volume reaches a steady value after a sufficient number of squeezes. The results of this numerical

simulation are illustrated in Figure 5.4, where it is specifically shown that this steady volume of liquid is reached after only three successive squeezes.
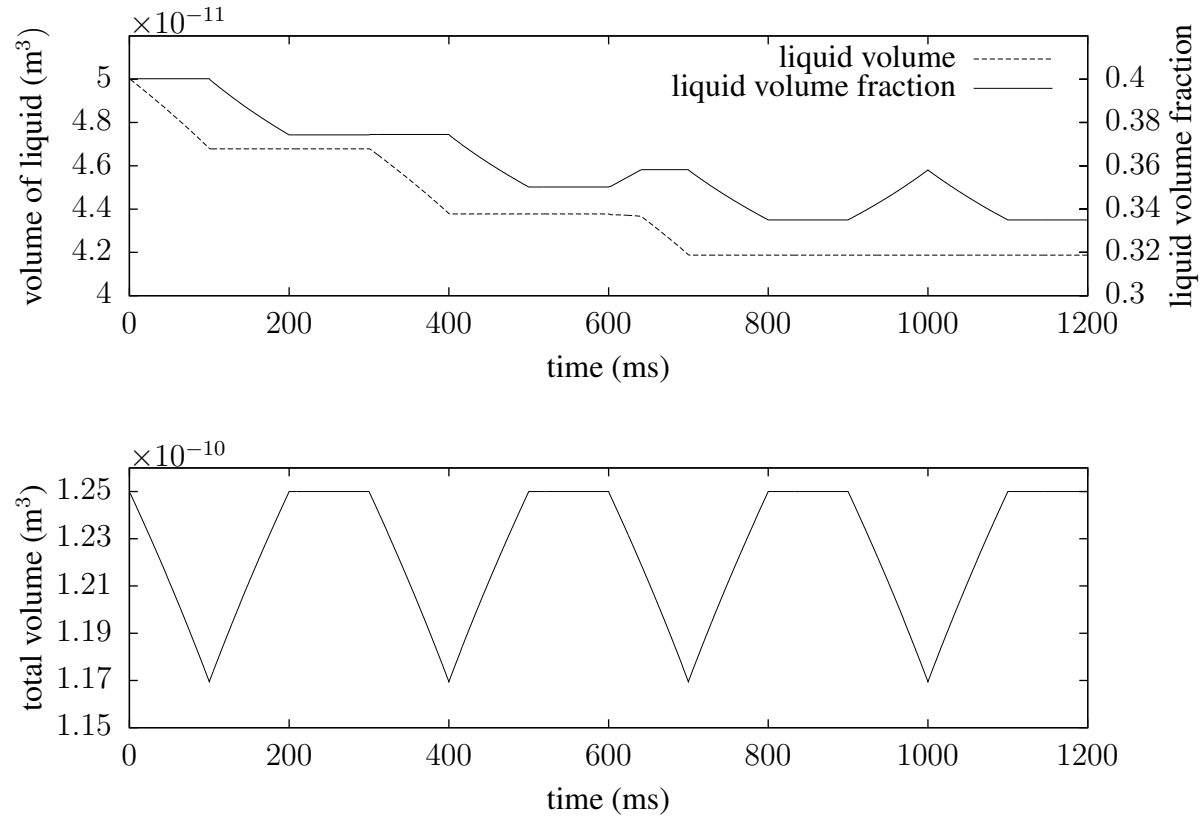
Figure 5.4: Squeezing of a saturated cube: Liquid and total volume as a function of time for the case of repeated squeezing

5.1.3 Flexure of a Nafion® film due to water absorption

It has been experimentally observed that when placing a water droplet on a dry thin film made of Nafion®, the region surrounding the droplet initially exhibits a bulge, which later disappears as the water evaporates and/or is diffused into the film [27]. To simulate this experiment, a water droplet is idealized by means of a prescribed liquid volume fraction boundary condition on a square region with 3 mm side at the center of the top surface of a $10 \times 10 \times 0.125$ mm Nafion® block. The latter is fixed on all of its four lateral faces and zero liquid flux boundary condition is imposed on all boundaries except for the droplet region. The supply of water is terminated at $t = 450$ s, at which

time the Dirichlet boundary condition $\phi = \bar{\phi}$ on the droplet region is replaced by a corresponding zero liquid flux condition. No attempt is made here to account for evaporation.

A uniform $20 \times 20 \times 5$ mesh is used for the analysis, and symmetry is exploited in modeling only a quarter of the domain. Also, the time step-size is set to $\Delta t = 0.2\,\text{s}$.
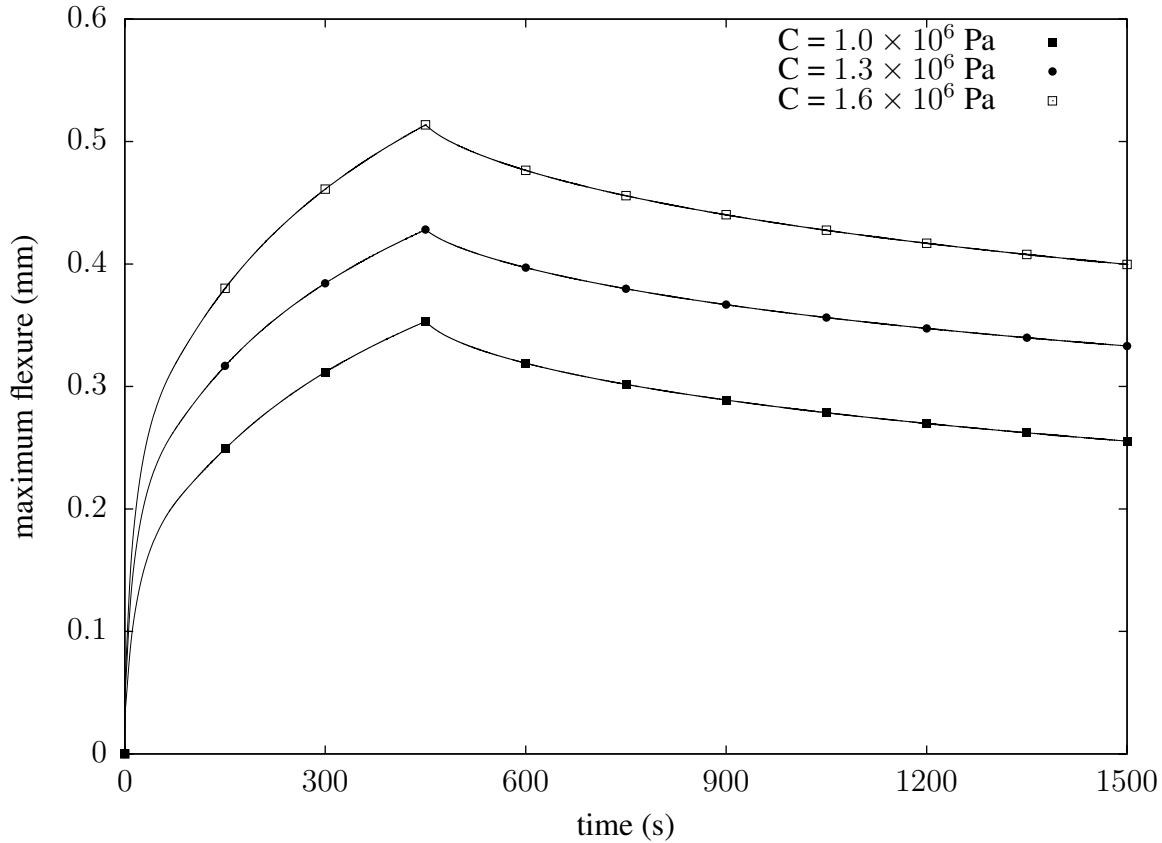
Figure 5.5: Flexure of a Nafion$^{\circledR}$ film due to water absorption: History of maximum flexure for three different values of the liquid pressure constant C

Figure 5.5 illustrates the flexure of the film at the center of water droplet for three different values of the liquid pressure constant C of equation (3.13). This is done to explore the predictive range of this variable, which, as stated earlier, is chosen without direct experimental evidence. It is noted that maximum flexure in the range of approximately $0.35\,\text{mm}$ to $0.51\,\text{mm}$ is achieved at $t = 450\,\text{s}$. After the water supply is terminated, the flexure starts decreasing with time. As seen in Figure 5.5, the maximum flexure increases with C, but the rate of its decrease after $t = 450\,\text{sec}$ appears to be independent of C. A contour plot of the transverse displacement at $t = 450\,\text{s}$ is illustrated in Figure 5.6 on the deformed configuration. These results are both qualitatively and quantitatively consistent with the experimental findings in [27], although the rate of decrease in

the maximum flexure appears to be significantly slower in the simulations.

DISPLACEMENT 3

|	
	-2.79E-09
	3.43E-05
	6.85E-05
	1.03E-04
	1.37E-04
	1.71E-04
	2.06E-04
	2.40E-04
	2.74E-04
	3.08E-04
	3.43E-04
	3.77E-04
	4.11E-04

Time = 4.50E+02
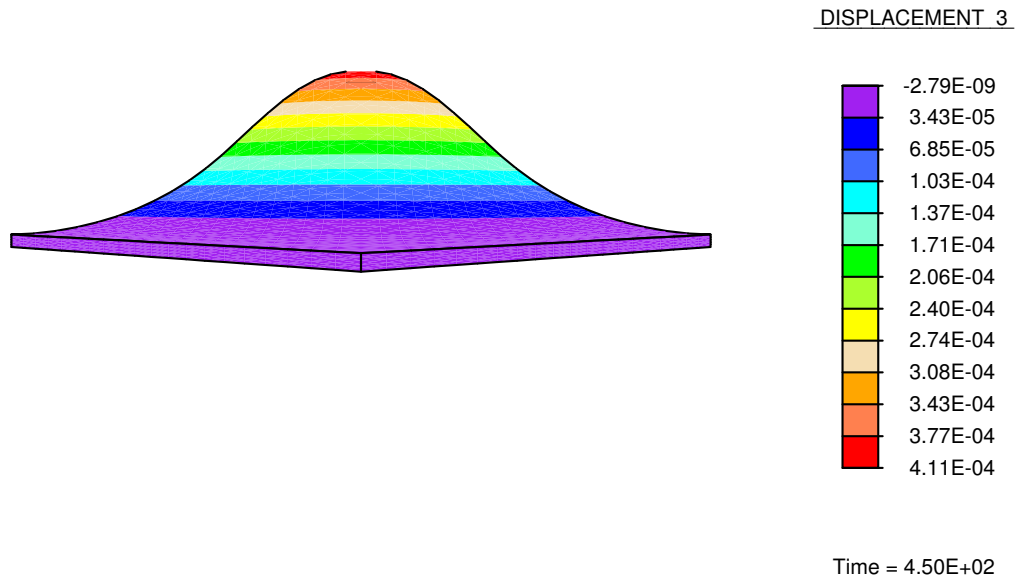
Figure 5.6: Flexure of a Nafion® film, in meters, due to water absorption: Deformed configuration and contour plot of transverse displacement (note that the displacement is magnified by a factor of 5)

5.2 Multiphase Diffusion in Porous Solid

The finite element formulation of the model described in Section 4.4 was implemented in the general-purpose nonlinear program FEAP. The model and its numerical implementation were tested on three representative simulations discussed below. All simulations employed 8-node isoparametric brick elements with full $2 \times 2 \times 2$ Gaussian quadrature. In addition, the time integration parameters defined in Section 5.1 were set to $\beta = 0.25$ and $\gamma = 0.5$.

5.2.1 The Leverett experiment
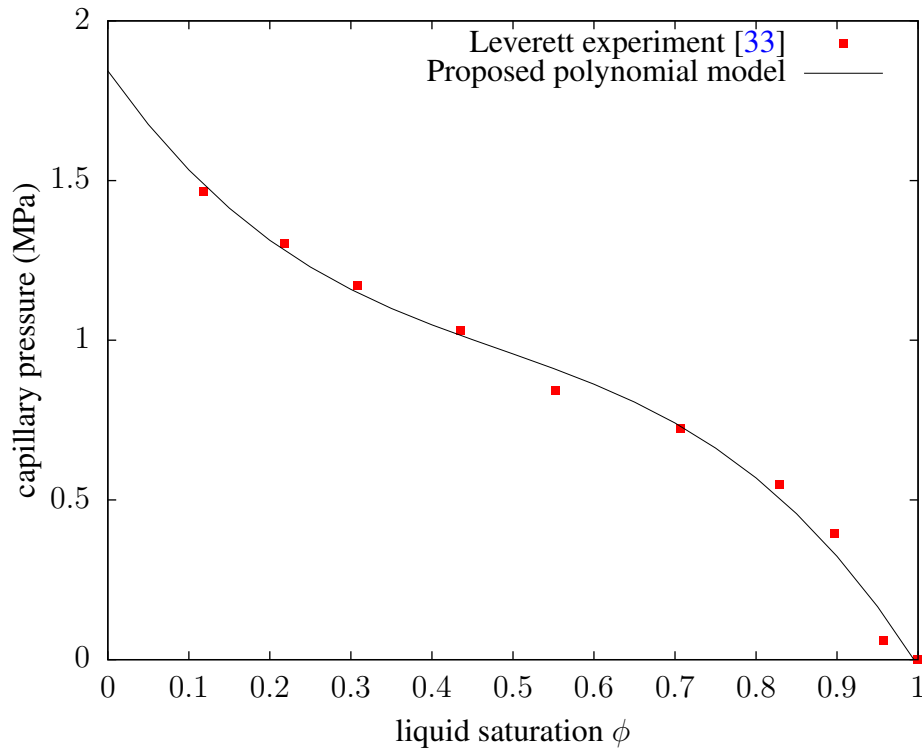
Figure 5.7: Capillary pressure as a function of liquid saturation for sand: polynomial fit of experimental data

The experiment of Leverett [33] is simulated here using the finite element implementation of the multiphase diffusion continuum model. In this experiment, a $0.05 \times 0.05 \times 6$ m tube is initially filled with dry soil (sand or clay). Next, water is supplied to the soil from the bottom of the tube at constant pressure, while the free surface of the soil is subjected to atmospheric pressure. Hence, water is imbibed into the soil due to capillary pressure. As noted in [33], after several weeks the water distribution reaches steady-state as the gravitational forces come to equilibrium with

capillary pressure. At that time, the saturation of the soil is measured at different levels in the tube and the corresponding capillary pressure is deduced from the elevations relative to the bottom of the tube.
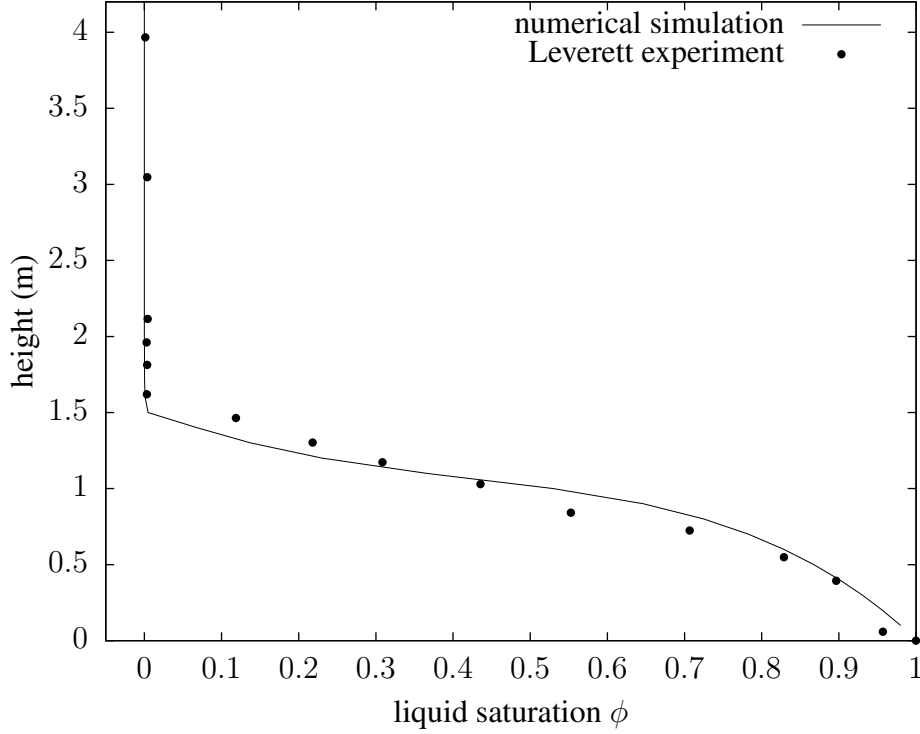
Figure 5.8: Leverett experiment: height of water as a function of the saturation in sand

Here, the Leverett experiment is considered for the case of sand saturated by water. Material properties for this experiment are taken from Table I in [33], and are $k_l = 3.60 \times 10^{-13}\,\text{m}^2$, $\mu_l = 1.0 \times 10^{-3}\,\text{Ns/m}^2$, $k_g = 3.63 \times 10^{-13}\,\text{m}^2$, $\mu_g = 1.5 \times 10^{-5}\,\text{Ns/m}^2$, and $\epsilon = 0.40$. The coefficients in the constitutive equation (4.17) are estimated from curve-fitting the experiment data in [33] for sand and water, such that

$$P_c = -3.9\phi^3 + 5.7\phi^2 - 3.6\phi + 1.8\,, \tag{5.2}$$

where P_c is calculated in MPa. The polynomial equation (5.2) and experiment data from [33] are plotted in Figure 5.7. A uniform $2 \times 2 \times 60$ block mesh is used to simulate the Leverett experiment with step-size of $\Delta t = 1000\,\text{s}$. The duration of the imbibition is taken to be 10 weeks. All macroscopic solid material are assumed to be stationary in space.

Figure 5.8 shows the water saturation at different heights in the tube at the end of the simulation. These results compare very well with the data in [33].

5.2.2 Squeezing of a saturated cube
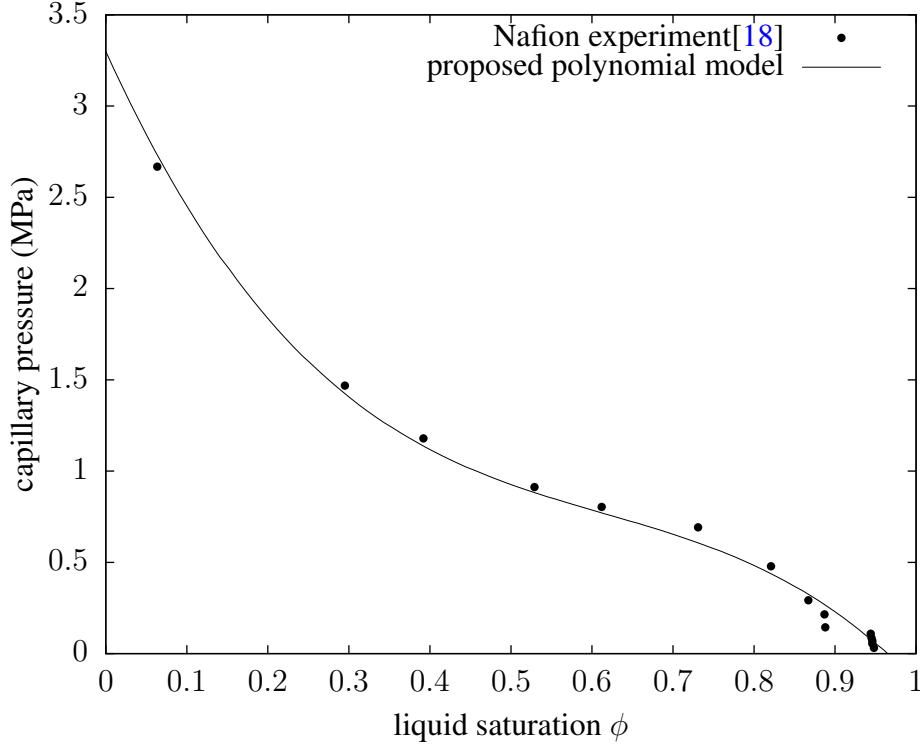
Figure 5.9: Capillary pressure as a function of liquid saturation for Nafion®: polynomial fit of experimental data

This simulation involves Nafion®. The material properties for the simulation are set to $\rho_s = 2 \times 10^3$ kgr/m³ [43], $\rho_l = 10^3$ kgr/m³, $\epsilon = 0.4$ [47], $k_l = 1.0 \times 10^{-13}$ m²/s, $\mu_l = 1.0 \times 10^{-3}$ Ns/m² for water [35], and $k_g = 0.75 \times 10^{-10}$ m²/s, $\mu_g = 2.0 \times 10^{-5}$ Ns/m² for oxygen [53]. Also, Nafion® is assumed to be hyperelastic and taken to obey the Kirchhoff-Saint Venant stress-strain law, and λ, μ are set to be $(\lambda, \mu) = (4.0, 2.7)$ MPa [43]. For constitutive equation (4.17), coefficients for Nafion® are obtained by curve fitting experiment data from Divisek [18], which leads to following expression

$$P_c = -7.8\phi^3 + 14.4\phi^2 - 10.2\phi + 3.6 \,, \tag{5.3}$$

where P_c is also calculated in MPa. Figure 5.9 illustrates that proposed cubic polynomial equation(5.3) matches the experiment data.

In Section 5.1, a computational experiment was proposed in which water is repeatedly squeezed out of a 0.5 mm cube of saturated Nafion® block. The porous solid is compressed uniformly on one of its faces using displacement control in the direction of compression, while the opposite face

remains fixed and each of the four lateral faces is free to slide on its own plane only. Liquid is allowed to exit from the compressed face, while all the other five faces are assumed impermeable.

The block is initially squeezed to 93% of its initial length while keeping the liquid saturation value of $\phi = 1$ on the compressed face. Then, it is stretched back to its original shape, where it is kept in rest until the liquid saturation reaches steady state. During the stretching and until steady state is attained, the compressed face is subject to zero liquid flux conditions. Each of three loading stages is imposed proportionally over a period of 0.1 s. The block is squeezed and stretched repeatedly, until enough liquid is pushed out of the block and a steady state of liquid saturation is reached. The simulation is carried out using a uniform $5 \times 5 \times 5$ mesh with step-size set to 1 ms.

Figure 5.10 illustrates the water is progressively drained with each squeeze and that it remains constant in volume during the stretching and resting stage. The figure also demonstrates that the total volume is reduced faster when compared to the corresponding result in [54], where the effect of gas is not modeled. Indeed, it is reasonable to assume that gas drives the liquid more vigorously from the block. It is also interesting to note that during the third squeeze the liquid saturation ϕ increases briefly before dropping to its final value. This is due to the fact that by this time the liquid content is already relatively low and the early stage of this squeeze generates reduction of the overall volume without removing any liquid.

Liquid diffusion appears to be relatively insensitive to the value of the gas permeability, as illustrated in Figure 5.11. Here, a full cycle of squeezing, stretching and resting of the same saturated Nafion$^{\circledR}$ cube is simulated using the original mesh and two different values of gas permeability, $k_g = 0.75 \times 10^{-10}$ m^2/s (the original value) and $k_g = 0.75 \times 10^{-9}$ m^2/s. A comparison of the total liquid volume during this cycle reveals negligible differences between the two simulations.

5.2.3 Flexure of a Nafion$^{\circledR}$ film due to water absorption

In Section 5.1, we attempted to simulate the flexure of a Nafion$^{\circledR}$ film with a water droplet placed on its top, which has been experimentally observed [27]. To simulate this experiment, a water droplet is idealized by means of a prescribed liquid saturation boundary condition on a square region with 3 mm side at the center of the top surface of a $10 \times 10 \times 0.125$ mm Nafion$^{\circledR}$ block. The latter is fixed on all of its four lateral faces and zero liquid flux boundary condition is imposed on all boundaries except for the droplet region. The supply of water is terminated at $t = 450$ s, at which time the Dirichlet boundary condition $\phi = 1$ on the droplet region is replaced by a corresponding zero liquid flux condition.

A uniform $20 \times 20 \times 5$ mesh is used for the analysis, and symmetry is exploited in modeling only a quarter of the domain. Also, the time step-size is set to 0.2 s.

Figure 5.12 illustrates the flexure of the film at the center of water droplet. It is noted that maximum flexure in the range of approximately 0.7 mm is achieved at $t = 450$ s. After the water supply is terminated, the flexure starts decreasing rapidly with time. These results are both qualitatively and quantitatively consistent with the experimental findings in [27]. Compared to the earlier attempt to simulate this experiment using single-phase diffusion, it is clear that the new two-phase
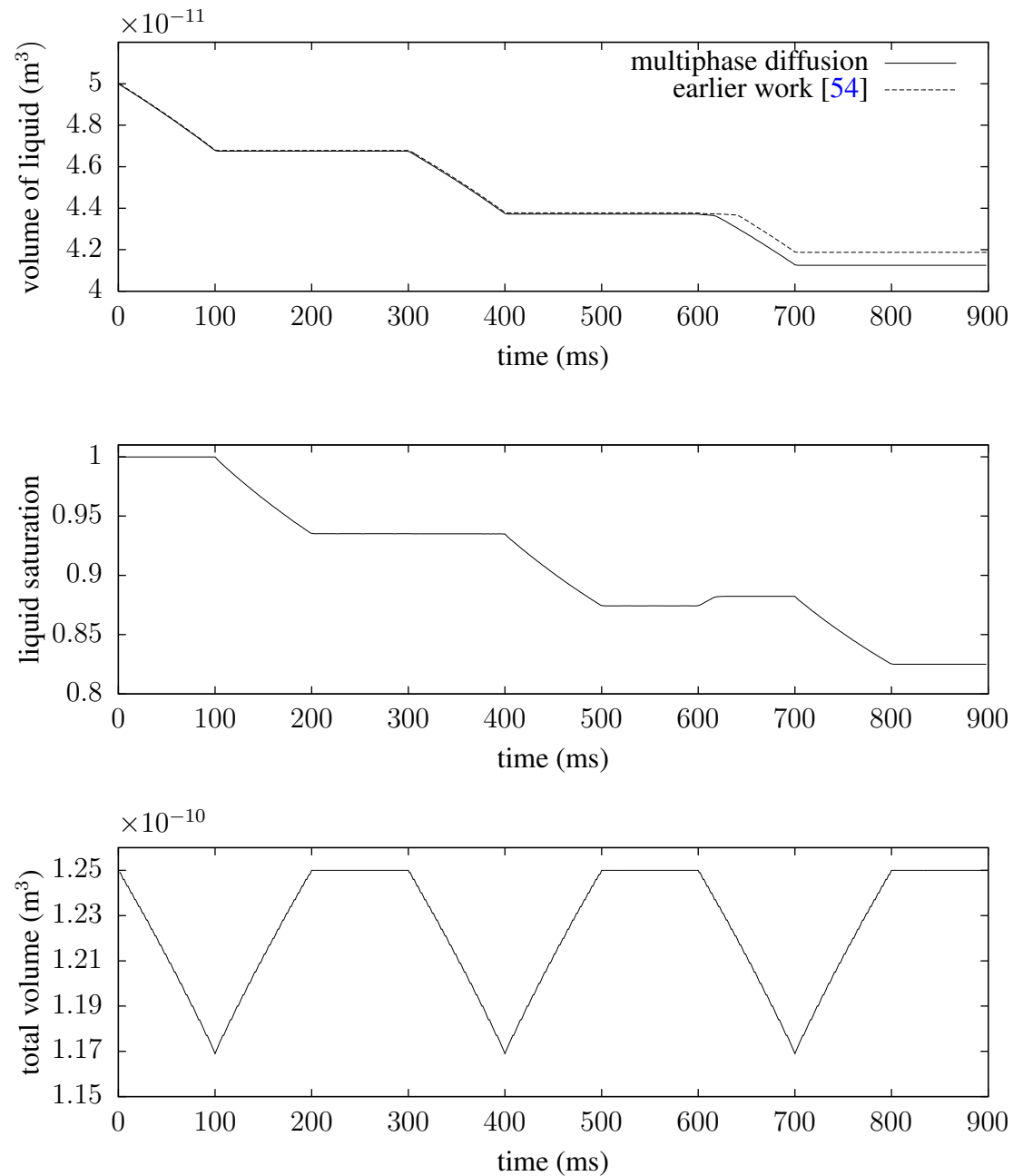
Figure 5.10: Squeezing of a saturated cube: Liquid and total volume as a function of time for the case of repeated squeezing
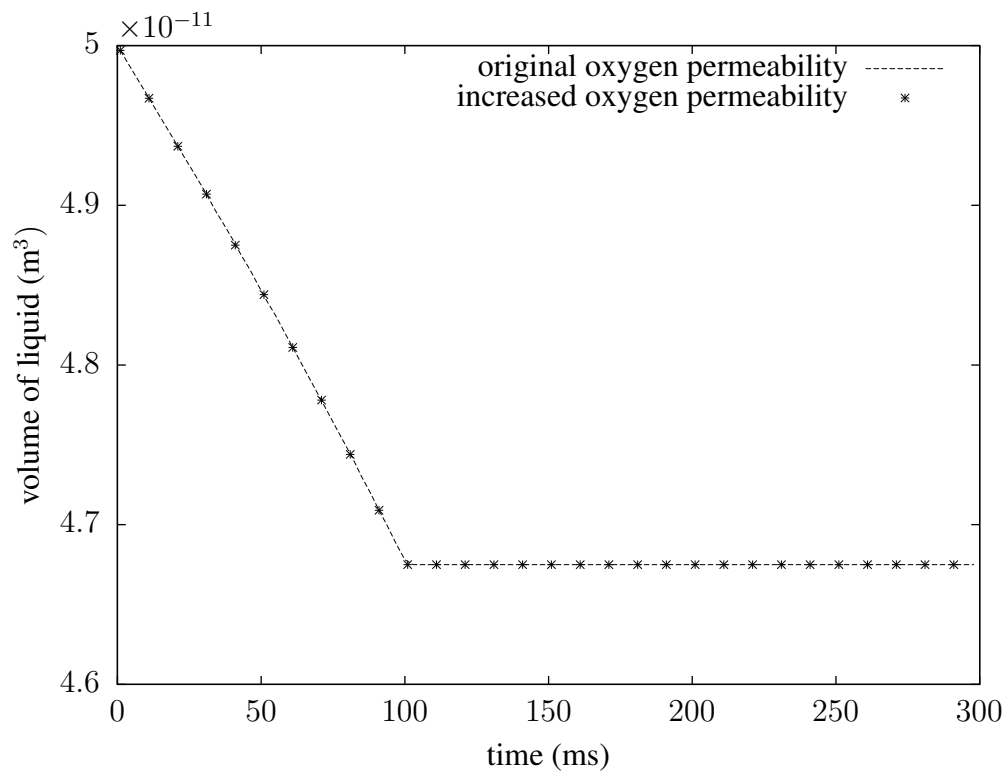
Figure 5.11: Comparison of two different value of oxygen permeability k_g: Liquid volume as a function of time for the case of squeezing

diffusion model is capable to model the rapid rate of decrease in the maximum flexure.
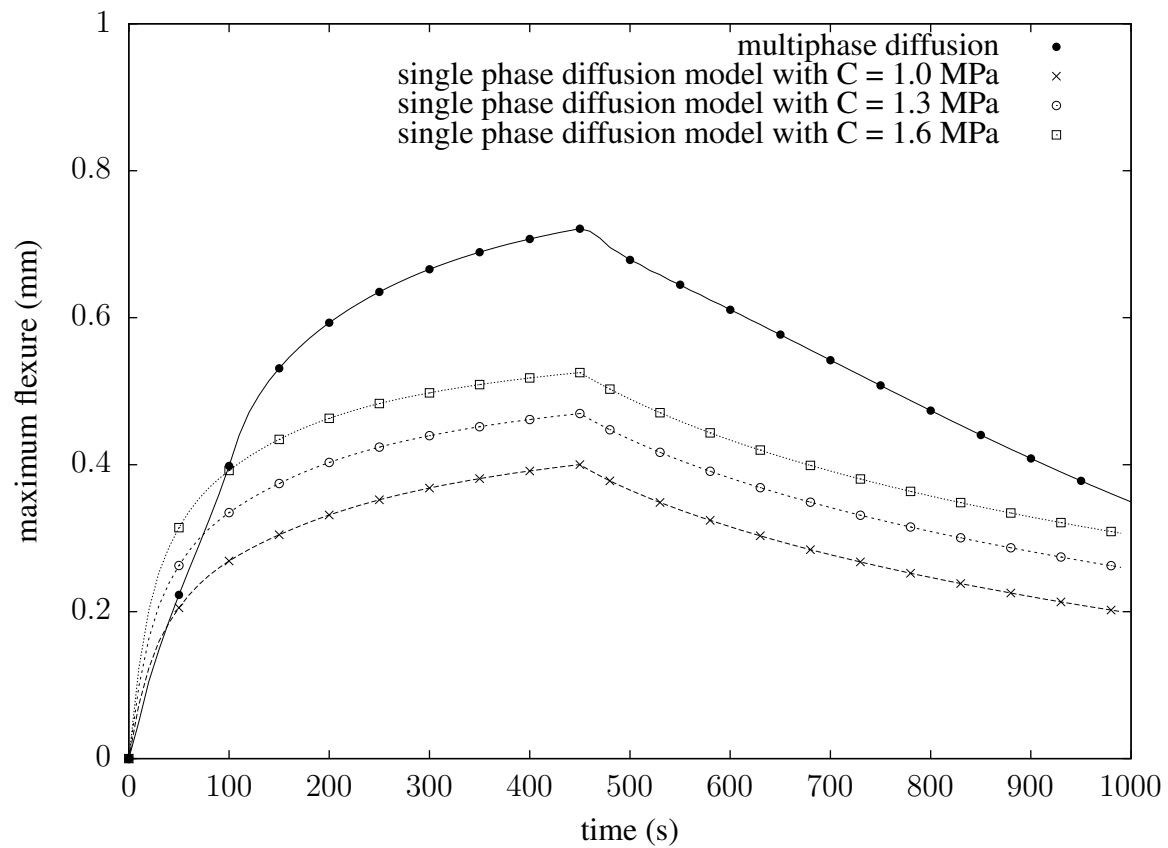
Figure 5.12: Flexure of a Nafion$^{®}$ film due to water absorption: comparison between multiphase diffusion model and previous model with three different liquid pressure constant C

5.3   Role of gas pressure in multiphase diffusion

The role of the gas phase in multiphase diffusion should be further studied, since gas can flow freely in microchannels formed by connected pores, inside the porous solid. In this section, we repeat all the three numerical simulation in Section 5.2 with uniform gas pressure, to simulate a free-flowing gas phase. All material properties and constitutive assumptions in Section 5.2 are used again here. Same mesh and time step size are also used. Same initial/boundary-conditions are used, except that pressure of the gas phase are fixed to be zero.

5.3.1   The Leverett experiment
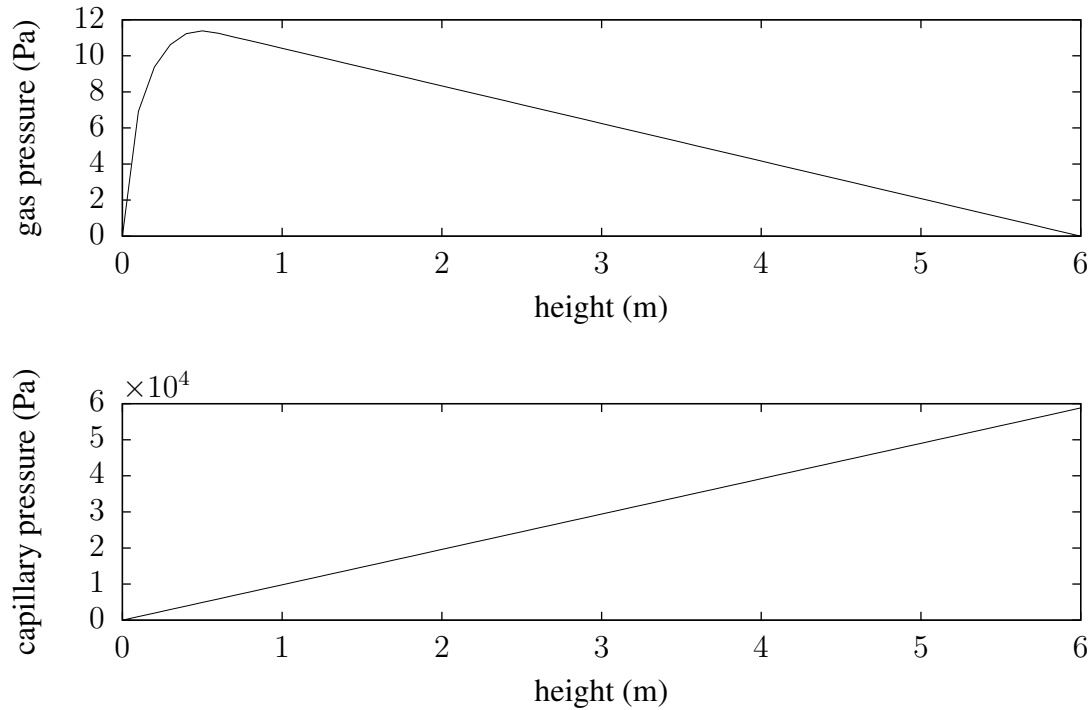
Figure 5.13: Gas pressure distribution in the tube compared to capillary pressure.

The experiment of Leverett [33] is simulated in Section 5.2 using the multiphase diffusion model. Here, we further explore the role of gas in this experiment.

Figure 5.13 shows air pressure distribution in the tube compared to capillary pressure at final steady state. Gas pressure is four order of magnitude smaller than capillary pressure.

Now, numerical simulation is repeated with gas pressure fixed to be zero in the whole tube. Figure 5.14 compares water saturation at different heights in the tube from the multiphase diffusion
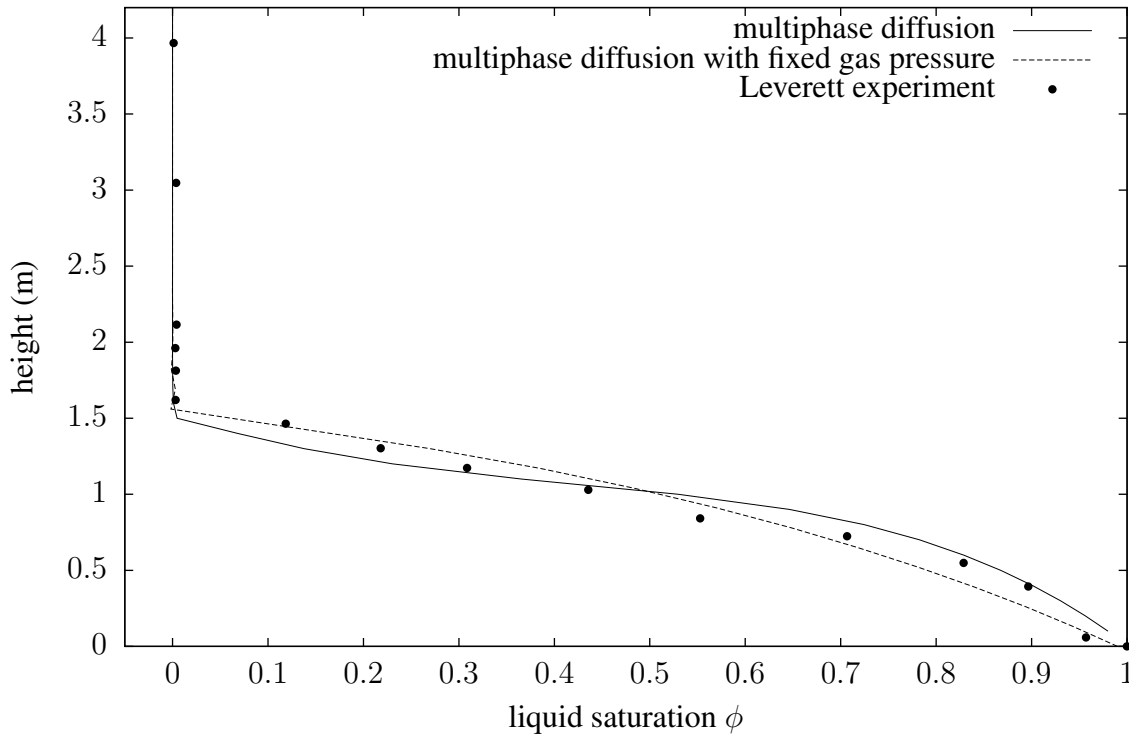
Figure 5.14: Leverett experiment: height of water as a function of the saturation in sand

model with free or fixed gas pressure to original experiment data. As illustrated in the figure, fixed gas pressure does suppress details in the numerical result, and matches the experiment data less accurately compared to the multiphase diffusion model with free gas phase.

5.3.2 Squeezing of a saturated cube

In Section 5.2, two numerical simulations were performed to simulate liquid and gas diffusion in deforming Nafion® block or film. Here, we will study the role of gas pressure in more detail by repeating the two simulations with gas pressure fixed to be zero. Figure 5.15 illustrates the water being squeezed out the Nafion® block, compares result of free gas pressure and fixed gas pressure. It clearly shows that liquid moves out of block more freely with free gas pressure than fixed zero gas pressure.

5.3.3 Flexure of a Nafion® film due to water absorption

Now, we will repeat the simulation of the flexure of a Nafion® film due to water absorption from Section 5.1 and 5.2. The multiphase diffusion model is used while gas pressure is fixed to be zero.

48
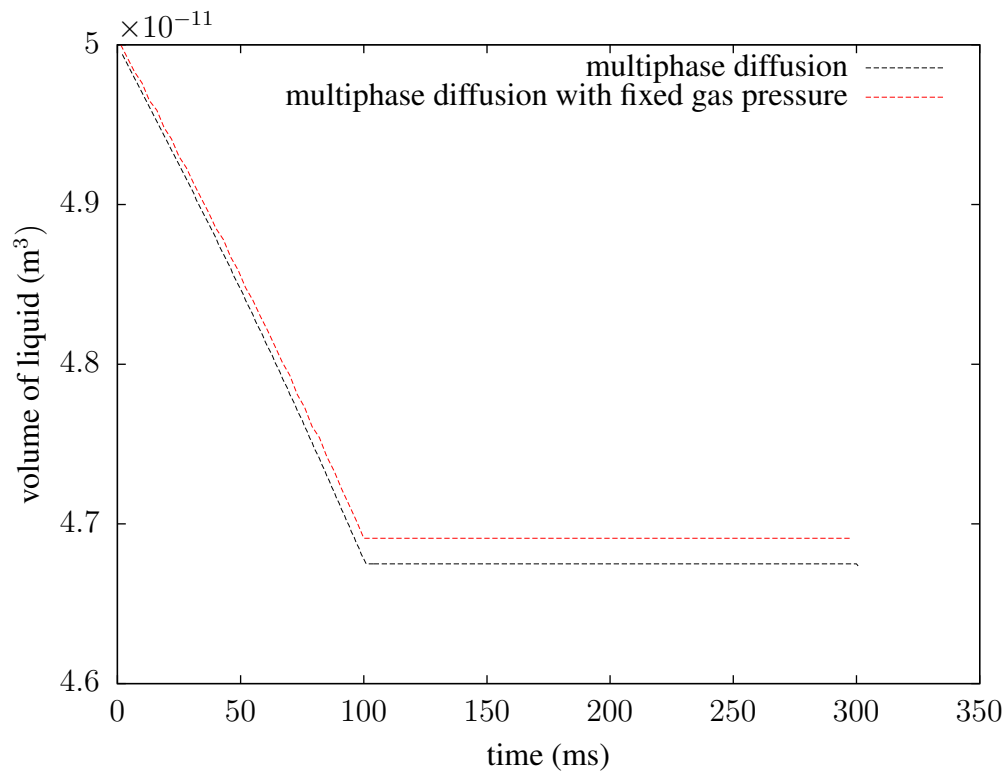
Figure 5.15: Squeezing of a saturated cube: Liquid volume as a function of time, multiphase diffusion result compared to result of fixed gas pressure
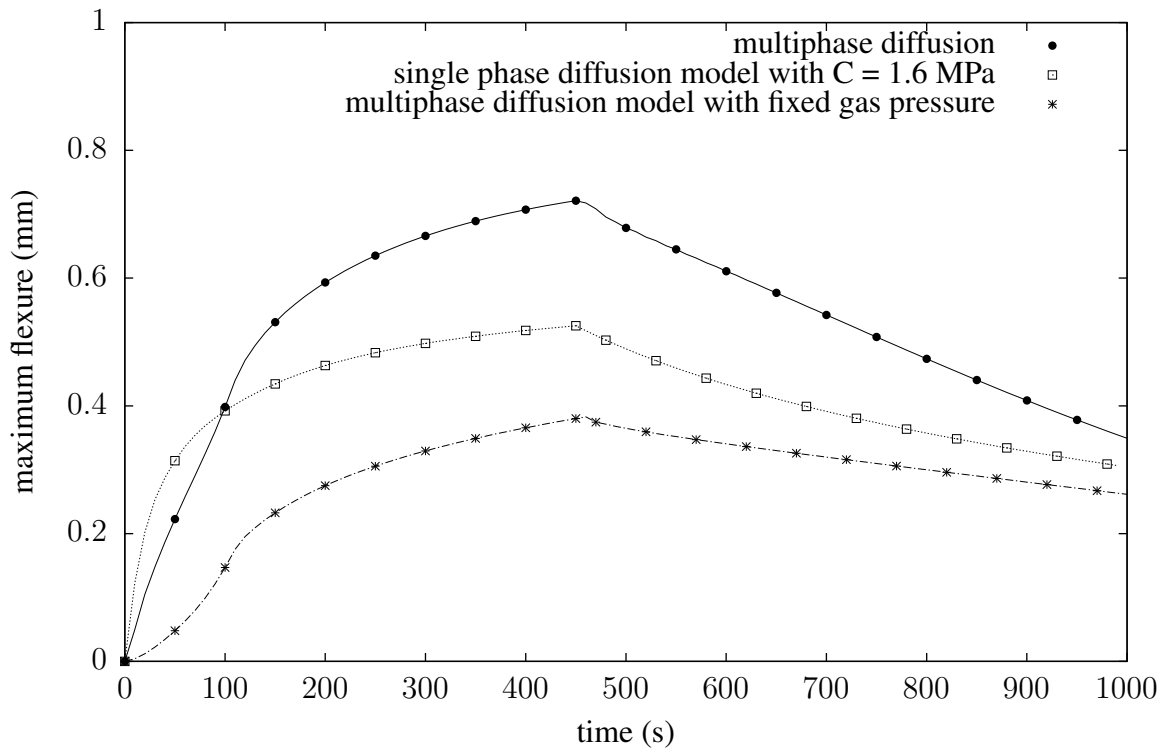
Figure 5.16: Flexure of a Nafion$^{\circledR}$ film due to water absorption: comparison between multiphase diffusion model, single phase diffusion model and fixed gas pressure.

Figure 5.16 compares three different results from single phase, multiphase model and multiphase model with zero gas pressure. It shows that multiphase diffusion model with zero gas pressure gives smallest maximum flexure when water supply is terminated at $t = 450\,$s. After the water supply is terminated, the rate of decrease of flexure is also much smaller than the other two models. Compared to other two models, lack of gas pressure makes water diffuse at a much slower rate, which is shown in both increase of flexure with water supply and decrease of flexure after water supply.

5.4 Linear approximation of Multiphase Diffusion Model

In Section 4.3, it is argued that a linear approximation of the constitutive equation for capillary pressure coupled with uniform gas pressure reduces the multiphase diffusion model to the single phase diffusion model. In this section, we will repeat the three numerical simulations in Section 5.2 with linear constitutive equation for capillary pressure and uniform gas pressure. The results will be compared with results from multiphase and single phase diffusion models.

5.4.1 Leverett experiment simulation
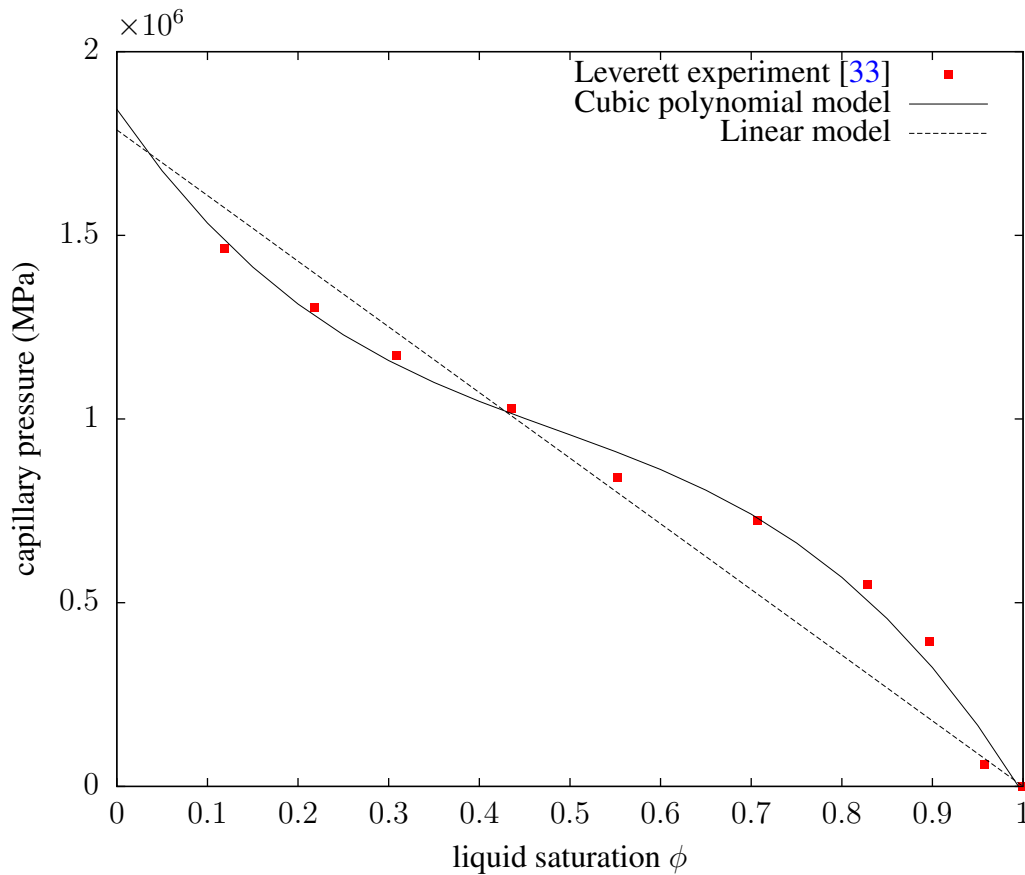
Figure 5.17: Capillary pressure as a function of liquid saturation for sand: Cubic polynomial fit and linear fit of experimental data

Numerical simulations of the water imbibition experiment of Leverett in Section 5.2 showed that the continuum model, with cubic polynomial constitutive relation between capillary pressure and liquid saturation, gives results which match satisfactorily the experiment data. Here, we will

attempt to use a linear approximation for the constitutive assumption for capillary pressure and repeat the simulation. A linear approximation of (4.17) is fitted to the original experiment data and the constitutive equation for capillary pressure reads as

$$P_c = 1.787(1 - \phi),$$ (5.4)

where P_c is calculated in MPa. Both linear and cubic polynomial constitutive equation are plotted
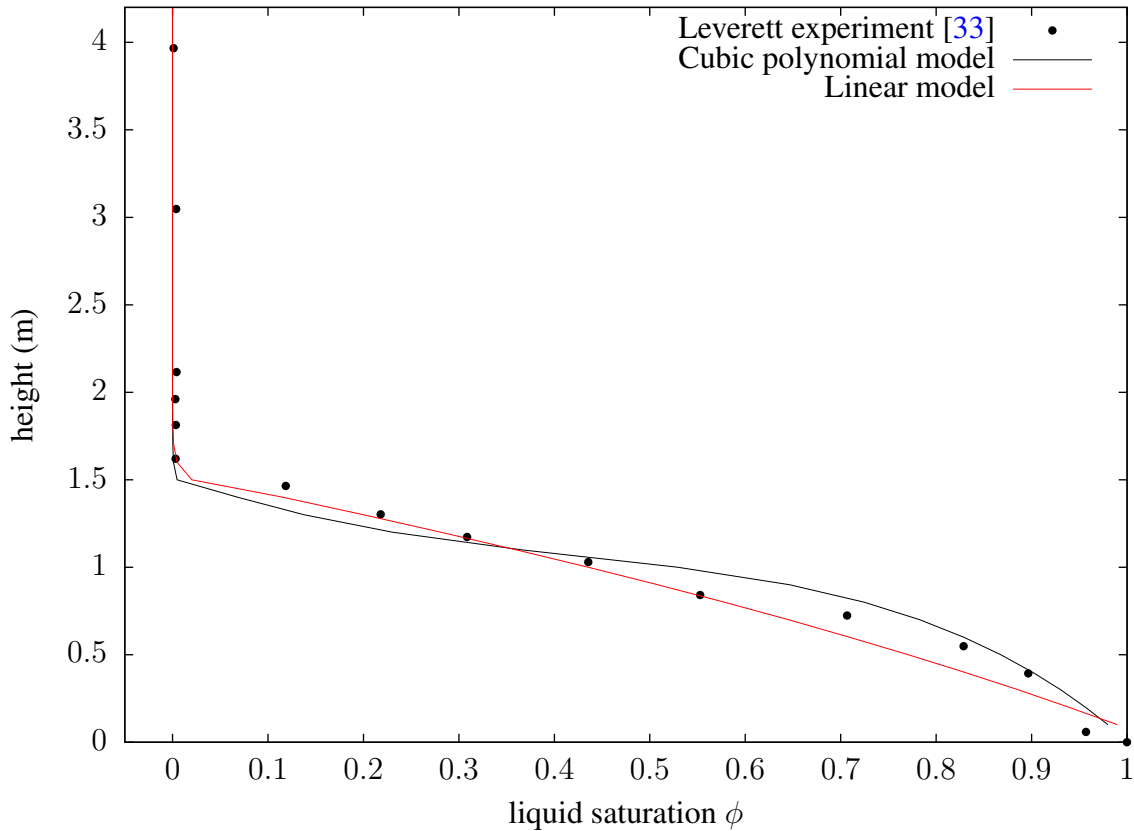
Figure 5.18: Leverett experiment

against experiment data in Figure 5.17. As shown in the figure, the linear approximation is fitted such that when liquid saturation is full ($\phi = 1$), the capillary pressure is equal to zero.

Again, the same material properties and uniform $2 \times 2 \times 60$ block mesh are used exactly as in Section 5.2. Water saturation is fixed to be 1 at the bottom of the long tube which is initially filled dry soil. The air pressure in this test is fixed to be zero throughout the tube. Figure 5.18 compares results from linear and cubic constitutive equations for capillary pressure and the original experiment data, and it shows that the linear constitutive equation produces numerical results that

match the overall shape of the experiment, but the cubic polynomial constitutive equation gives more accurate numerical result around full saturation area (i.e. $\phi = 1$).

5.4.2 Squeezing a saturated cube
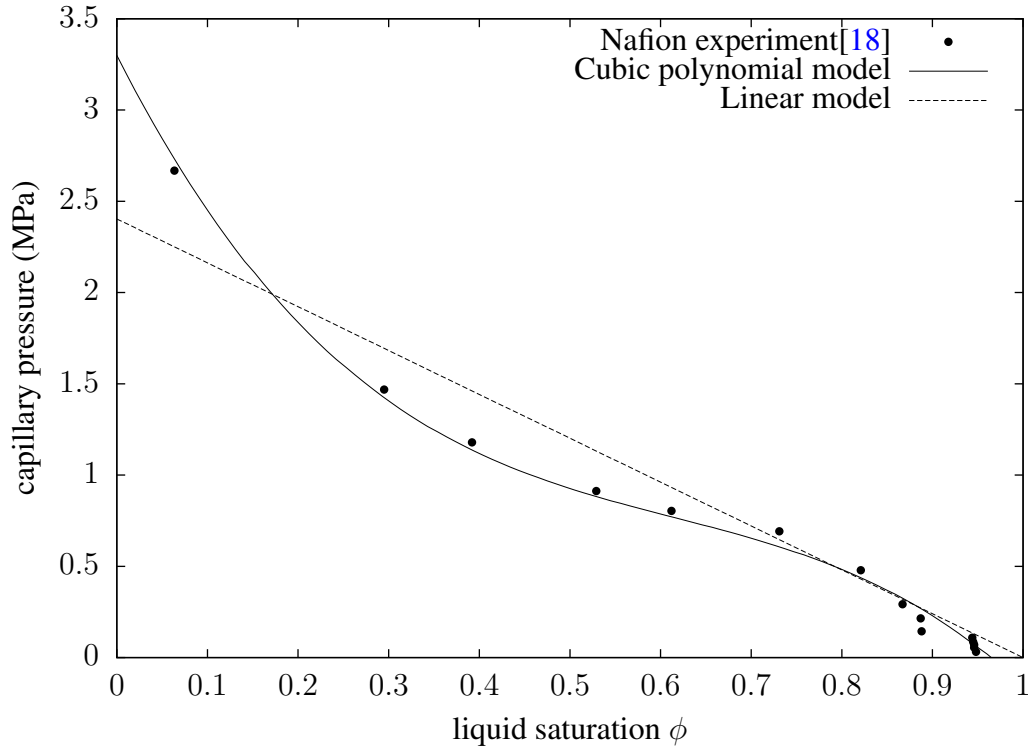
Figure 5.19: Capillary pressure as a function of liquid saturation for Nafion$^{\circledR}$: Cubic polynomial fit and linear fit of experimental data

In Section 5.2, we modeled water being squeezed repeatedly out of a saturated Nafion$^{\circledR}$ cube using multiphase diffusion continuum model with cubic polynomial constitutive equation for capillary pressure. Here, the linear constitutive model is fitted to the experiment data of capillary pressure and liquid saturation for Nafion$^{\circledR}$ from [18], and reads

$$P_c = 2.403(1 - \phi) \text{ MPa} . \tag{5.5}$$

Both cubic and linear constitutive model are plotted against experiment data in Figure 5.19.

Next, the numerical simulation is repeated to model water being squeezed out of a 0.5 mm cube of saturated Nafion$^{\circledR}$. The cube is compressed on one of its faces using displacement control, while

the opposite face is fixed and all four lateral faces are free to slide on their own plane. Gas pressure are fixed to be zero uniform in the whole cube.
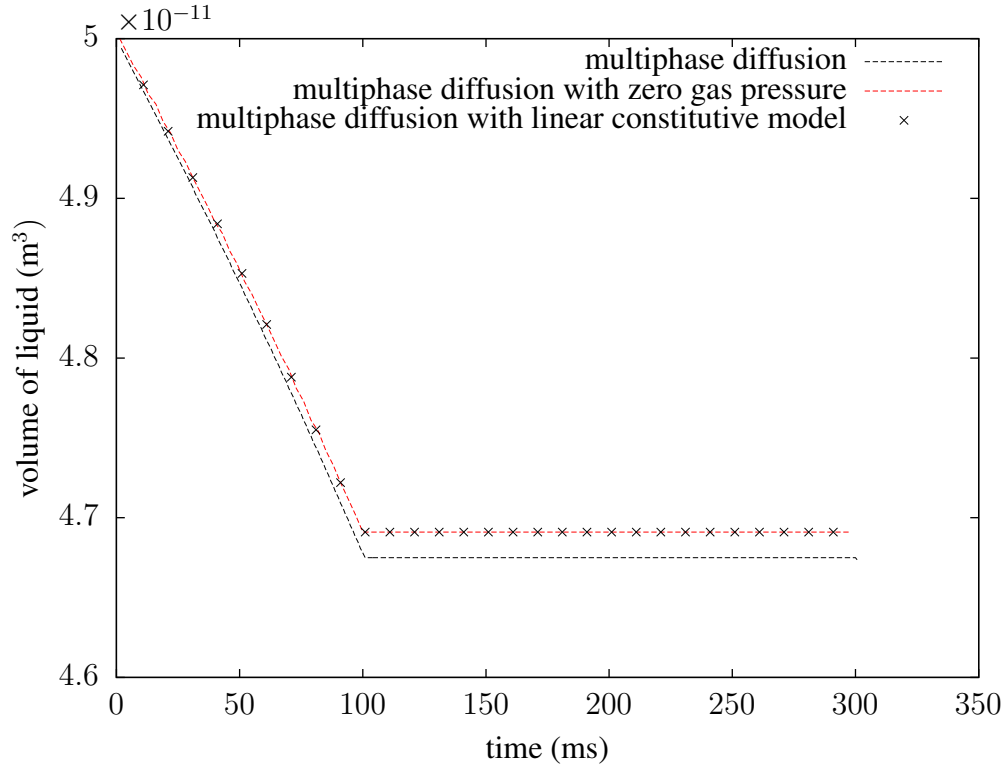
Figure 5.20: Squeezing of a saturated cube: liquid volume as a function of time

To illustrate the difference between the cubic and linear constitutive assumption, free and fixed gas pressure, three different results are plotted in Figure 5.20. It shows that fixed zero gas pressure will decrease the amount of water squeezed out of the cube, and cubic and linear forms of constitutive equation for capillary pressure give results with negligible difference.

5.4.3 Flexure of Nafion® film

Simulation of the flexure of Nafion® film due to water absorption is carried out both in Section 5.1 and 5.2. While single diffusion model can successfully achieve the maximum flexure of the Nafion® film, the multiphase diffusion model outperform the single diffusion model by reproducing the steep decreasing rate of the flexure after termination of water supply.

Now we incorporate the linear model of constitutive equation (5.5) for capillary pressure. Same uniform $20 \times 20 \times 5$ mesh is used to simulate a $10 \times 10 \times 0.125$ mm Nafion® film. Water droplet is modeled by a prescribed liquid saturation boundary condition of $\phi = 1$ on a square region

with 3 mm side. Nafion film is fixed on all of its four lateral faces and zero liquid flux boundary condition. Gas pressure is fixed to be zero in the whole domain. Water supply is terminated at $t = 450$ seconds by switching the Dirichlet boundary condition to zero flux boundary condition. Figure 5.21 illustrate the flexure of the Nafion® film at the center of water droplet. It is noted that
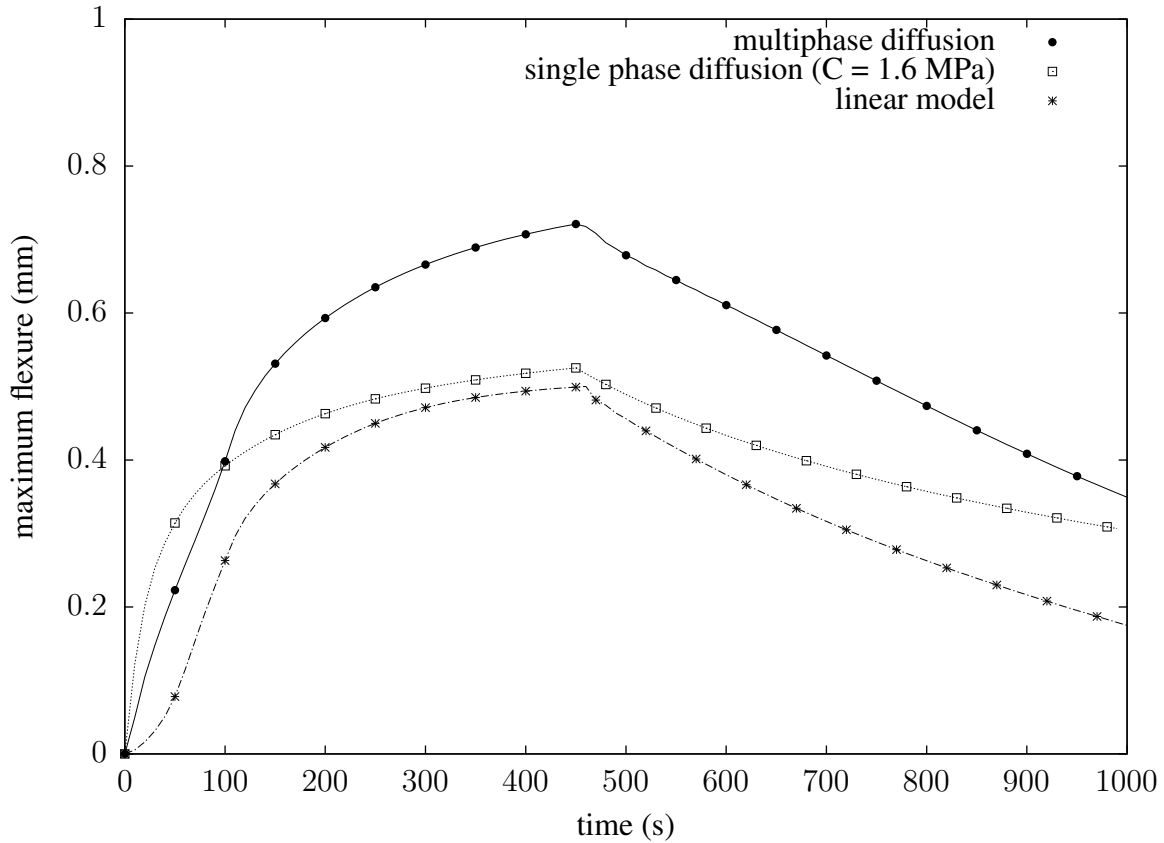
Figure 5.21: Capillary pressure as a function of liquid saturation for Nafion®: Cubic polynomial fit and linear fit of experimental data

the maximum flexure for linear model is close to the single diffusion model, but the decrease rate of flexure after 450 seconds is similar to the multiphase diffusion model.

Chapter 6

Conclusions

The principal goal of this study is to enable the modeling of fluid flow in elastic porous solids undergoing finite deformation in the presence of time- and space-varying fluid concentration. Both single phase and multiphase continuum-mechanical models proposed here satisfy the preceding imperatives, while allowing for the imposition of meaningful boundary conditions on displacement and liquid/gas concentration. For both models, the choice of state variables results in minimum number of degrees of freedom per finite element node, and the formulation of the governing equations results in the elimination of the fluid velocity from the system of equations. By not including fluid velocity or displacement as state variable, the need of imposing fluid traction boundary condition is also avoided, which is of major practical importance, as such conditions are not easy to plausibly set. Capillary effects are also modeled in the multiphase diffusion model, and constitutive relation between capillary pressure and liquid saturation is studied.

The numerical simulations on Nafion$^{\circledR}$ demonstrate the predictive power of the two proposed models, both of which give intuitively correct responses to simple loading conditions, such as stretching and squeezing under various saturation conditions. In addition, the simulation of Leverett's sand imbibition experiment validates that J-function is suitable constitutive assumption for capillary pressure. All numerical simulations are also repeated with gas pressure fixed to be zero to study the role of gas in multiphase diffusion model, and it is shown in all simulations that gas does play an important role in multiphase diffusion, and appears to drive liquid diffusion more vigorously. Both models capture the experimentally observed flexure of a Nafion$^{\circledR}$ film caused by a droplet of water on top surface, and multiphase diffusion model gives the steep decreasing rate of flexure after termination of water supply, which is more accurate than the single phase diffusion model. Additionally, an alternative linear form of constitutive assumption for capillary pressure is tested with all numerical simulations, which all show that the linear assumption may furnish reasonably close result numerically, but not as accurate as the cubic form of constitutive assumption.

Further work remains to be done in exploring the nature of the non-linearity in the constitutive relation between liquid saturation and capillary pressure. Temperature should also be included in

the model.

Bibliography

[1] J.E. Adkins. Non-linear diffusion: I. diffusion and flow of mixture of fluids. *Philosophical Transactions of the Royal Society A*, 255:607–633, 1963.

[2] J.E. Adkins. Non-linear diffusion: II. Constitutive equations for mixtures of isotropic fluids. *Philosophical Transactions of the Royal Society A*, 255:635–648, 1963.

[3] J.E. Adkins. Non-linear diffusion: III. Diffusion through isotropic highly elastic solids. *Philosophical Transactions of the Royal Society A*, 256:301–316, 1964.

[4] A.E.Green and P.M.Naghdi. A theory of mixtures. *Archive for Rational Mechanics and Analysis*, 24:243–263, 1967.

[5] A.E.Green and P.M.Naghdi. On basic equations of mixture. *Quarterly Journal of Mechanics and Applied Mathematics*, 22:427–438, 1969.

[6] R.J. Atkin and R.E. Craine. Continuum theories of mixtures: Basic theory and historical development. *Quarterly Journal of Mechanics and Applied Mathematics*, 29:209–244, 1976.

[7] Y. Bachmat and J. Bear. Macroscopic modelling of transport phenomena in porous media. 1: The continuum approach. *Transport in Porous Media*, 21:213–240, 1986.

[8] T. Berning and N. Djilali. A 3d, multiphase, multicomponent model of cathode and anode of a pem fuel cell. *Journal of The Electrochemical Society*, 150:1589–1598, 2003.

[9] R.M. Bowen. Toward a thermodynamics and mechanics of mixtures. *Archive for Rational Mechanics and Analysis*, 24(5):370–403, 1967.

[10] R.M. Bowen. Incompressible porous media models by use of the theory of mixtures. *International Journal of Engineering Science*, 18:1129–1148, 1980.

[11] R.M. Bowen. Compressible porous media models by use of the theory of mixtures. *International Journal of Engineering Science*, 20:697–735, 1982.

[12] R.H. Brooks and A.T. Corey. *Hydraulic Properties of Porous Media*. Colorado State University, Fort Collins, 1964.

[13] R.E. Collins. *Flow of Fluids through Porous Materials*. Penn Well Books, Tulsa, OK.

[14] O. Coussy. A general theory of thermoporoelastoplasticity for saturated porous materials. *Transport in Porous Media*, 4(3):281–293, 1989.

[15] O. Coussy. *Poromechanics*. John Wiley and Sons, Chichester, 2004.

[16] O. Coussy, R Eymard, and T. Lassabatere. Constitutive modeling of unsaturated drying deformable materials. *Journal of Engineering Mechanics*, 124(6):658–667, 1998.

[17] H. Darcy. *Les fontaines publiques de la ville de Digon*. V. Dalmont, 1856.

[18] J. Divisek, M. Eikerling, V. Mazin, H. Schmitz, U. Stimming, and Y.M. Volfkovich. A study of capillary porous structure and sorption properties of nafion proton-exchange membranes swollen in water. *Journal of The Electrochemical Society*, 145(8), 1998.

[19] N. Djilali. Computational modeling of polymer electrolyte membrane (pem) fuel cells: challenges and opportunities. *Energy*, 32(4):269–280, 2007.

[20] J.A. Elliott, S. Hanna, A.M.S. Elliott, and G.E. Cooley. The swelling behaviour of perfluorinated ionomer membranes in ethanol/water mixtures. *Polymer*, 42:2251–2253, 2001.

[21] A. Fick. On liquid diffusion. *Philosophical Magazine*, 10(63):30–39, 1855.

[22] D.J. Gargas, D.A. Bussian, and S.K. Buratto. Investigation of connectivity of hydrophilic domains in Nafion using electrochemical pore-directed nanolithography. *Nano Letters*, 5:2184–2187, 2005.

[23] D. Gawin, P. Baggio, and B.A. Schrefler. Coupled heat, water and gas flow in deformable porous media. *International Journal for Numerical Methods in Fluids*, 20(E2):969–987, 1995.

[24] D. Gawin, B.A. Schrefler, and M. Galino. Thermo-hydro-mechanical analysis of partially saturated porous materials. *Engineering Computations*, 13(7):113–143, 1996.

[25] M.Th.van Genuchten. A closed-formed equation for predicting the hydraulic conductivity of unsaturated soils. *Soil Science Society of America Journal*, 44(5):892–898, 1980.

[26] J. Ghaboussi and E.L. Wilson. Flow of compressible fluid in porous elastic media. *International Journal for Numerical Methods in Engineering*, 5:419–442, 1973.

[27] S. Goswami, S. Klaus, and J.B. Benziger. Wetting and absorption of water drops on Nafion films. *Langmuir*, 24(16):8627–8633, 2008.

[28] S.M. Hassanizadeh and W.G. Gray. General conservation equations for multiphase systems: 1. Averaging procedure. *Advances in Water Resources*, 2(4):131–144, 1979.

[29] S.M. Hassanizadeh and W.G. Gray. General conservation equations for multiphase systems: 3. Constitutive theory for porous media flow. *Advances in Water Resources*, 3:25–40, 1980.

[30] S.M. Hassanizadeh and W.G. Gray. General conservation equations for multiphase systems: 2. Mass, momenta, energy and entropy. *Advances in Water Resources*, 2(4):191–203, 1990.

[31] J. Korsawe, G. Starke, W. Wang, and O. Kolditz. Finite element analysis of poro-elastic consolidation in porous media: standard and mixed approaches. *Computer Methods in Applied Mechanics and Engineering*, 195:1096–1115, 2006.

[32] M.C. Leverett. Capillary behavior in porous solids. *Transaction of the AIME*, 142(1):152–169, 1941.

[33] M.C. Leverett, W.B. Lewis, and M.E. True. Dimensional-model studies of oil-field behavior. *Transaction of the AIME*, 146:175–193, 1942.

[34] K.A. Mauritz and R.B. Moore. State of understanding of Nafion. *Chemical Reviews*, 104:4535–4586, 2004.

[35] S. Motupally, A.J. Becker, and J.W. Weidner. Diffusion of water in Nafion 115 membranes. *Journal of the Electrochemical Society*, 147:3171–3177, 2000.

[36] N.M. Newmark. A method of computation in structural dynamics. *ASCE Journal of Engineering Mechanics*, 85:67–94, 1959.

[37] T.V. Nguyen and M.W. Knobbe. A liquid water management strategy for pem fuel cell stacks. *Journal of Power Sources*, 114:70–79, 2003.

[38] T.V. Nguyen and R.E. White. A water and heat management model for proton-exchange-membrane fuel cells. *Journal of the Electrochemical Society*, 140:2178–2186, 1993.

[39] U. Pasaogullari and C.Y. Wang. Two phase transport and the role of micro-porous layer in polymer electolyte fuel cell. *Electrochimica Acta*, 49:4359–4369, 2004.

[40] K.R. Rajagopal and L. Tao. *Mechanics of Mixture*. World Properties, Singapore, 1995.

[41] K.R. Rajagopal, A.S. Wineman, and M. Gandhi. On boundary conditions for a certain class of problem in mixture theory. *International Journal of Engineering Science*, 24:1453–1463, 1986.

[42] J. Rutqvist, L. BÖrgesson, M. Chijimatsu, A. Kobayashi, L Jing, T.S. Nguyen, J. Noorishad, and C.F. Tsang. Thermohydromechanics of partially saturated geological media: governing equations and formulation of four finite element models. *International Journal of rock mechanics and mining sciences*, 38(1):105–127, 2001.

[43] M.B. Satterfield, P.W. Mjsztrik, H. Ota, J.B. Benziger, and A.B. Bocarsly. Mechanical properties of Nafion and Titania/Nafion composite membranes for polymer electrolyte membrane fuel cells. *Journal of Polymer Science Part B: Polymer Physics*, 44(16):2327–2345, 2006.

[44] B.A. Schrefler. Mechanics and thermodynamics of saturated/unsaturated porous materials and quantitative solutions. *Applied Mechanics Reviews*, 55(4):351–388, 2002.

[45] B.A. Schrefler and X. Zhan. A fully coupled model for water flow and airflow in deformable media. *Water Resources Research*, 29(1):155–167, 1003.

[46] B.A. Schrefleri, X. Zhan, and L. Simoni. A coupled model for water flow, airflow and heat flow in deformable porous media. *International Journal of Numerical Methods for heat fluid flow*, 5(6):531–547, 1995.

[47] S. Song, W. Zhou, J. Tian, and R. Cai. Ethanol crossover phenomena and its influence on performance of DEFC. *Journal of Power Sources*, 145:266–271, 2005.

[48] R.L. Taylor. *FEAP - A Finite Element Analysis Program, Programmer Manual*. University of California, Berkeley. http://www.ce.berkeley.edu/feap.

[49] R.L. Taylor. *FEAP - A Finite Element Analysis Program, User Manual*. University of California, Berkeley. http://www.ce.berkeley.edu/feap.

[50] Clifford Truesdell. Sulle basi della termomeccanica. *Rend, Lincei*, 22(33):158–158, 1957.

[51] K.S. Udell. Heat transfer in porous media considering phase change and capillarity - the heat pipe effect. *International Journal of Heat Mass Transfer*, 28(2):485–495, 1985.

[52] Adam Z Weber and John Newman. Modeling transport in polymer-electrolyte fuel cells. *Chemical Reviews-Columbus*, 104(10):4679–4726, 2004.

[53] L. Zhang, C. Ma, and S. Mukerjee. Oxygen permeation studies on alternative proton exchange membranes designed for elevated temperature operation. *Electrochimica Acta*, 48:1845–1859, 2003.

[54] Q. Zhao and P. Papadopoulos. Modeling and simulation of liquid diffusion through a porous finitely elastic solid. *Computational Mechanics*, 1:1–10, 2013.

Appendix A

Single Phase Diffusion Finite Element Implementation: Consistent Linearization

In this appendix, expressions are recorded for the consistent element tangent stiffness matrix required by the Newton-Raphson method to determine the nodal displacements and pressures from the weak forms (3.23) and (3.27) in conjunction with the time integration equations (3.34). To this end, let the element interpolations at time t_{n+1} be given by $\mathbf{u}_{n+1} = \sum_{I=1}^{N} N_I \hat{\mathbf{u}}_{I_{n+1}}$, $\phi_{n+1} = \sum_{I=1}^{N} N_I \hat{\phi}_{I_{n+1}}$, $\boldsymbol{\xi}_{n+1} = \sum_{J=1}^{N} N_J \hat{\boldsymbol{\xi}}_{J_{n+1}}$, $\eta_{n+1} = \sum_{J=1}^{N} N_J \hat{\eta}_{J_{n+1}}$, where N_I, $I = 1, 2, \ldots, N$, denote the I-th element interpolation function and the superscript "$\hat{(\cdot)}_I$" signifies the value of a variable $(\cdot)$ at node I. For brevity, the subscript $n + 1$ is suppressed in the remainder of the appendix.

The linearization of the weak forms (3.23) and (3.27) for a typical element e gives rise to a tangent stiffness matrix of the form

$$\begin{bmatrix} K \end{bmatrix} = \begin{bmatrix} \begin{bmatrix} K^{\phi u} \end{bmatrix} & \begin{bmatrix} K^{\phi\phi} \end{bmatrix} \\ \begin{bmatrix} K^{uu} \end{bmatrix} & \begin{bmatrix} K^{u\phi} \end{bmatrix} \end{bmatrix} , \tag{A.1}$$

where the $N \times 3N$ submatrix $\begin{bmatrix} K^{\phi u} \end{bmatrix}$ and the $N \times N$ submatrix $\begin{bmatrix} K^{\phi\phi} \end{bmatrix}$ result from the linearization of the mass balance equation (3.23) in the direction of $\hat{\mathbf{u}}$ and $\hat{\phi}$, respectively. Likewise, the $3N \times 3N$ submatrix $\begin{bmatrix} K^{uu} \end{bmatrix}$ and the $3N \times N$ submatrix $\begin{bmatrix} K^{u\phi} \end{bmatrix}$ are due to the linearization of the momentum balance equation (3.27) along the same directions.

Taking into account (3.23) and (3.34), it can be easily shown that

$$K_{I(jJ)}^{\phi u} = \frac{\gamma}{\beta \Delta t} \int_{\Omega^e} \rho_l \phi N_I N_{J,j} \, dv \tag{A.2}$$

and

$$
\begin{aligned}
K_{IJ}^{\phi\phi} &= \frac{1}{\gamma\Delta t}\int_{\Omega^e}\rho_l N_I N_J\,dv \\
&\quad + \int_{\Omega^e}\rho_l N_I N_J\,\mathrm{div}\,\mathbf{v}\,dv \\
&\quad + \int_{\Omega^e}K\rho_l\sum_{k=1}^{3}(N_{I,k}(\phi N_{J,k}+N_J\phi_{,k})\,dv\,,
\end{aligned}
\tag{A.3}
$$

where $j,k=1,2,3$ are spatial coordinate indices, $N_{I,j}$ is the partial derivative of N_I with respect to the spatial coordinate x_j, and Ω^e is the element domain.

Correspondingly, starting from (3.27) and (3.34), it is found that

$$
\begin{aligned}
K_{(iI)(jJ)}^{uu} &= \frac{1}{\beta\Delta t^2}\int_{\Omega^e}N_I\rho N_J\delta_{ij}\,dv \\
&\quad + \frac{\gamma}{\beta\Delta t}\int_{\Omega^e}(\sum_{k=1}^{3}N_I q_k N_{J,k})\delta_{ij}\,dv \\
&\quad + \frac{\gamma}{\beta\Delta t}\int_{\Omega^e}N_I q_i N_{J,j}\,dv \\
&\quad + K_{(iI)(jJ)}^{m}
\end{aligned}
\tag{A.4}
$$

and

$$
\begin{aligned}
K_{(iI)J}^{u\phi} &= \int_{\Omega^e}N_I\rho_l N_J\frac{dv_i}{dt}\,dv \\
&\quad + \int_{\Omega^e}K\sum_{k=1}^{3}(-K\rho_l\phi_{,i}N_{I,k}(N_J\phi_{,k}+\phi N_{J,k})+N_{I,i}N_{J,k}q_k)\,dv \\
&\quad - \int_{\Omega^e}K\rho_l N_I\sum_{k=1}^{3}(v_{i,k}(\phi N_{J,k}+N_J\phi_{,k}))\,dv \\
&\quad - \int_{\Omega^e}K\rho_l N_I(\phi N_{J,i}+N_J\phi_{,i})\,\mathrm{div}\,\mathbf{v}\,dv \\
&\quad - \int_{\Omega^e}K\rho_l N_I(N_J\frac{d\phi_{,i}}{dt}+\frac{1}{\gamma\Delta t}\phi N_{J,i}+\frac{1}{\gamma\Delta t}N_I\phi_{,i}+\frac{d\phi}{dt}N_{J,i})\,dv\,,
\end{aligned}
\tag{A.5}
$$

where $i,j,k=1,2,3$ are spatial coordinate indices. Also, $K_{(iI)(jJ)}^{m}$ denotes the material tangent stiffness emanating from the stress-divergence term in (3.27).

Appendix B

Multiphase Diffusion Finite Element Implementation: Consistent Linearization

Consistent linearization of the weak forms (4.22), (4.23) and (3.27) is required for the solution of the non-linear balance laws using the Newton-Raphson method at a given time t_{n+1}. To this end, and after time discretization by (4.26), let the interpolation for element e be $\phi_{n+1} = \sum_{I=1}^{N} N_I^e \hat{\phi}_{I\,n+1}$, $p_{g\,n+1} = \sum_{I=1}^{N} N_I^e \hat{p}_{g\,I\,n+1}$, and $\mathbf{u}_{n+1} = \sum_{I=1}^{N} N_I^e \hat{\mathbf{u}}_{I\,n+1}$ for the dependent variables, and, likewise, $\eta_{n+1} = \sum_{I=1}^{N} N_I^e \hat{\eta}_{I\,n+1}$, $\zeta_{n+1} = \sum_{I=1}^{N} N_I^e \hat{\zeta}_{I\,n+1}$, and $\boldsymbol{\xi}_{n+1} = \sum_{I=1}^{N} N_I^e \hat{\boldsymbol{\xi}}_{I\,n+1}$ for the test functions. Here, again, N_I^e denotes the I-th element interpolation function of element e and the superscript "$\hat{(\cdot)}_I$" signifies the value of variable $(\cdot)$ at node I. Once more, the subscript $n+1$ is omitted in the rest of this appendix for brevity.

The linearization of the weak forms (4.22), (4.23) and (4.25) gives rise to an element tangent stiffness matrix $\begin{bmatrix} K^e \end{bmatrix}$ of the form

$$\begin{bmatrix} K^e \end{bmatrix} = \begin{bmatrix} \begin{bmatrix} K^{\phi\phi} \end{bmatrix} & \begin{bmatrix} K^{\phi p} \end{bmatrix} & \begin{bmatrix} K^{\phi u} \end{bmatrix} \\ \begin{bmatrix} K^{p\phi} \end{bmatrix} & \begin{bmatrix} K^{pp} \end{bmatrix} & \begin{bmatrix} K^{pu} \end{bmatrix} \\ \begin{bmatrix} K^{u\phi} \end{bmatrix} & \begin{bmatrix} K^{up} \end{bmatrix} & \begin{bmatrix} K^{uu} \end{bmatrix} \end{bmatrix} . \tag{B.1}$$

Here, the $N \times N$ submatrix $\begin{bmatrix} K^{\phi\phi} \end{bmatrix}$, the $N \times N$ submatrix $\begin{bmatrix} K^{\phi p} \end{bmatrix}$ and the $N \times 3N$ submatrix $\begin{bmatrix} K^{\phi u} \end{bmatrix}$ result from the linearization of the liquid mass balance equation (4.22) in the directions of the increments $\Delta\hat{\phi}_I$, $\Delta\hat{p}_I$ and $\Delta\hat{\mathbf{u}}_I$, $I = 1, 2, \ldots, N$, of the dependent nodal variables. Likewise, the $N \times N$ submatrix $\begin{bmatrix} K^{p\phi} \end{bmatrix}$, the $N \times N$ submatrix $\begin{bmatrix} K^{pp} \end{bmatrix}$, and the $N \times 3N$ submatrix $\begin{bmatrix} K^{pu} \end{bmatrix}$ result from the linearization of the gas mass balance equation (4.23), while the $3N \times N$ submatrix $\begin{bmatrix} K^{u\phi} \end{bmatrix}$, the $3N \times N$ submatrix $\begin{bmatrix} K^{up} \end{bmatrix}$ and the $3N \times 3N$ submatrix $\begin{bmatrix} K^{uu} \end{bmatrix}$ result from the linearization of the momentum balance equation (4.25) along the same directions. Explicit expressions are provided below for all the submatrices. In these expressions, the variables i, j, k are associated the spatial coordinates x_i, x_j, x_k, respectively.

It can be easily deduced from the linearization of (4.22) that the components of the first row of

submatrices in (B.1) are

$$
\begin{aligned}
K_{IJ}^{\phi\phi} &= \int_{\Omega^e} \rho_l \epsilon N_I^e N_J^e \, dv + \int_{\Omega^e} \rho_l \epsilon N_I^e N_J^e \operatorname{div} \mathbf{v} \, dv \\
&+ \sum_{k=1}^{3} \int_{\Omega^e} N_{I,k}^e \rho_l \frac{k_l}{\mu_l} \epsilon \Big(N_J^e \big(p_{,k} + \frac{dP_c}{d\phi} \phi_{,k} \big) + \phi \big(\frac{dP_c}{d\phi} N_{J,k}^e + \frac{d^2 P_c}{d\phi^2} N_J^e \phi_{,k} \big) \Big) \, dv \, , \quad \text{(B.2)}
\end{aligned}
$$

$$
K_{IJ}^{\phi p} = \sum_{k=1}^{3} \int_{\Omega^e} N_{I,k}^e \rho_l \frac{k_l}{\mu_l} \epsilon \phi N_{J,k}^e \, dv \, , \tag{B.3}
$$

and

$$
K_{I(jJ)}^{\phi u} = \frac{\gamma}{\beta \Delta t} \int_{\Omega^e} \rho_l \epsilon \phi N_I^e N_{J,j}^e \, dv \, . \tag{B.4}
$$

Here, $N_{J,j}^e$ is the partial derivative of N_J^e with respect to the spatial coordinate x_j and Ω^e is the domain of element e.

Similarly, the linearization of (4.23) yields

$$
\begin{aligned}
K_{IJ}^{p\phi} &= -\frac{\gamma}{\beta \Delta t} \int_{\Omega^e} \rho_g \epsilon N_I^e N_J^e \, dv - \int_{\Omega^e} \rho_g \epsilon N_I^e N_J^e \operatorname{div} \mathbf{v} \, dv \\
&+ \sum_{k=1}^{3} \int_{\Omega^e} N_{I,k}^e \rho_g \frac{k_g}{\mu_g} \epsilon N_J^e p_{g,k} \, dv \, , \quad \text{(B.5)}
\end{aligned}
$$

$$
K_{IJ}^{pp} = \sum_{k=1}^{3} \int_{\Omega^e} N_{I,k}^e \rho_g \frac{k_g}{\mu_g} \epsilon (1 - \phi) N_{J,k}^e \, dv \, , \tag{B.6}
$$

and

$$
K_{I(jJ)}^{pu} = \frac{\gamma}{\beta \Delta t} \int_{\Omega^e} \rho_g \epsilon (1 - \phi) N_I^e N_{J,j}^e \, dv \, . \tag{B.7}
$$

Lastly, upon linearization of (4.25) it follows that

$$
\begin{aligned}
K^{u\phi}_{(iI)J} &= \int_{\Omega^e} N^e_I \rho_l N^e_J \frac{dv_i}{dt}\, dv + \int_{\Omega^e} \frac{k_g}{\mu_g} N^e_I \rho_g N^e_J \sum_{k=1}^{3} \big(v_{i,k} p_{g,k}\big)\, dv \\
&+ \sum_{k=1}^{3} \int_{\Omega^e} N^e_I \rho_l \frac{k_l}{\mu_l}\Big(v_{i,k}\epsilon N^e_J(p_{g,k} + \frac{dP_c}{d\phi}\phi_{,k}) + \phi\frac{d^2 P_c}{d\phi^2} N^e_J \phi_{,k} + \phi\frac{dP_c}{d\phi} N^e_{J,k}\Big)\, dv \\
&- \int_{\Omega^e} \frac{k_g}{\mu_g}\rho_g N^e_I \epsilon N^e_J p_{g,i} \operatorname{div} \mathbf{v}\, dv \\
&+ \int_{\Omega^e} \frac{k_l}{\mu_l}\rho_l N^e_I \epsilon\Big(N^e_J(p_{g,i} + \frac{dP_c}{d\phi}\phi_{,i}) + \phi(\frac{d^2 P_c}{d\phi^2} N^e_J \phi_{,i} + \frac{dP_c}{d\phi} N^e_{J,i})\Big) \operatorname{div} \mathbf{v}\, dv \\
&- \frac{1}{\gamma\Delta t}\int_{\Omega^e} \frac{k_g}{\mu_g}\rho_g N^e_I \epsilon N^e_J p_{g,i}\, dv \\
&- \int_{\Omega^e} \frac{k_l}{\mu_l}\rho_l N^e_I \Big(\frac{1}{\gamma\Delta t} N^e_J(p_{g,i} + \frac{dP_c}{d\phi}\phi_{,i}) + \frac{d\phi}{dt}\frac{dP_c}{d\phi} N^e_{J,i} + \frac{d\phi}{dt}\frac{d^2 P_c}{d\phi^2} N^e_J \phi_{,i}\Big)\, dv \\
&- \int_{\Omega^e} \frac{k_l}{\mu_l}\rho_l \epsilon N^e_I N^e_J\big(\frac{dp_{,i}}{dt} + \frac{dP_c}{d\phi}\frac{d\phi_{,i}}{dt} + \frac{d^2 P_c}{d\phi^2}\frac{d\phi}{dt}\phi_{,i}\big)\, dv \\
&- \int_{\Omega^e} \frac{k_l}{\mu_l}\rho_l \epsilon N^e_I \phi\big(\frac{d^2 P_c}{d\phi^2}\frac{d\phi_{,i}}{dt} N^e_J + \frac{1}{\gamma\Delta t}\frac{dP_c}{d\phi} N^e_{J,i} + \frac{1}{\gamma\Delta t}\frac{d^2 P_c}{d\phi^2} N^e_J \phi_{,i} + \frac{d^2 P_c}{d\phi^2}\frac{d\phi}{dt} N^e_{J,i}\big)\, dv \\
&- \int_{\Omega^e} \frac{k_g}{\mu_g}\phi_{,i} N^e_{I,k}\big(\frac{k_g}{\mu_g}\rho_g \epsilon N^e_J p_{g,k}\big)\, dv + \int_{\Omega^e} \frac{k_l}{\mu_l}\big(\frac{dP_c}{d\phi} N^e_{J,i} + \frac{d^2 P_c}{d\phi^2}\big)\sum_{k=1}^{3}\big(N^e_{I,k}(q_l)_k\big)\, dv \\
&+ \int_{\Omega^e} \frac{k_l}{\mu_l}(p_{,i} + \frac{dP_c}{d\phi}\phi_{,i})\sum_{k=1}^{3} N^e_{I,k}\Big(-\frac{k_l}{\mu_l}\rho_l \epsilon\big(N^e_J(p_{g,k} + \frac{dP_c}{d\phi}\phi_{,k}) + \phi\frac{dP_c}{d\phi} N^e_{J,k} + \phi\frac{d^2 P_c}{d\phi^2} N^e_J \phi_{,k}\big)\Big)\, dv\ ,
\end{aligned}
$$

(B.8)

$$
\begin{aligned}
K^{up}_{(iI)J} &= -\sum_{k=1}^{3} \int_{\Omega^e} N_I^e v_{i,k} \frac{k_g}{\mu_g} \rho_g \epsilon (1-\phi) N_{J,k}^e \, dv - \sum_{k=1}^{3} \int_{\Omega^e} N_I^e v_{i,k} \frac{k_l}{\mu_l} \rho_l \epsilon \phi N_{J,k}^e \, dv \\
&\quad - \int_{\Omega^e} N_I^e \frac{k_g}{\mu_g} \rho_g \epsilon (1-\phi) N_{J,i}^e \operatorname{div} \mathbf{v} \, dv - \int_{\Omega^e} N_I^e \frac{k_l}{\mu_l} \rho_l \epsilon \phi N_{J,i}^e \operatorname{div} \mathbf{v} \, dv \\
&\quad - \int_{\Omega^e} N_I^e \frac{k_g}{\mu_g} \rho_g \epsilon \Big(\frac{1}{\gamma \Delta t} (1-\phi) N_{J,i}^e - \frac{d\phi}{dt} N_{J,i}^e \Big) dv - \int_{\Omega^e} N_I^e \frac{k_l}{\mu_l} \rho_l \epsilon \Big(\frac{d\phi}{dt} N_{J,i}^e + \phi N_{J,i}^e \frac{1}{\gamma \Delta t} \Big) dv \\
&\quad + \int_{\Omega^e} \frac{k_g}{\mu_g} \sum_{k=1}^{3} \Big(N_{J,i}^e N_{I,k}^e (q_g)_k - p_{g,i} N_{I,k}^e \frac{k_g}{\mu_g} \rho_g \epsilon (1-\phi) N_{J,k}^e \Big) dv \\
&\quad + \int_{\Omega^e} \frac{k_l}{\mu_l} \sum_{k=1}^{3} \Big(N_{J,i}^e N_{I,k}^e (q_l)_k - \big(p_{g,i} + \frac{dP_c}{d\phi} \phi_{,i} \big) N_{I,k}^e \frac{k_l}{\mu_l} \rho_l \epsilon \phi N_{J,k}^e \Big) dv \,,
\end{aligned}
\tag{B.9}
$$

and

$$
\begin{aligned}
K^{uu}_{(iI)(jJ)} &= \frac{1}{\beta \Delta t^2} \int_{\Omega^e} N_I^e \rho N_J^e \delta_{ij} \, dv + \frac{\gamma}{\beta \Delta t} \int_{\Omega^e} \Big(\sum_{k=1}^{3} N_I^e (q_g)_k N_{J,k}^e \Big) \delta_{ij} \, dv \\
&\quad + \frac{\gamma}{\beta \Delta t} \int_{\Omega^e} \Big(\sum_{k=1}^{3} N_I^e (q_l)_k N_{J,k}^e \Big) \delta_{ij} \, dv + \frac{\gamma}{\beta \Delta t} \int_{\Omega^e} N_I^e (q_g)_i N_{J,j}^e \, dv \\
&\quad + \frac{\gamma}{\beta \Delta t} \int_{\Omega^e} N_I^e (q_l)_i N_{J,j}^e \, dv + K^m_{(iI)(jJ)} \,,
\end{aligned}
\tag{B.10}
$$

where $K^m_{(iI)(jJ)}$ denotes the material tangent stiffness from the stress-divergence term in (4.25) and δ_{ij} is the Kronecker symbol.